

‘Mathematical’ Cracks Versus Artificial Slits: Implications in the Determination of Fracture Toughness

Ch. F. Markides¹ · S. K. Kourkoulis¹

Received: 4 April 2015 / Accepted: 9 July 2015 / Published online: 11 August 2015
© Springer-Verlag Wien 2015

Abstract An analytic solution is introduced for the stress field developed in a circular finite disc weakened by a central slit of arbitrary ratio of its edges and slightly rounded corners. The disc is loaded by radial pressure applied along two finite arcs of its periphery, anti-symmetric with respect to the disc’s center. The motive of the study is to consider the stress field in a disc with a mechanically machined slit (finite distance between the two lips) in juxtaposition to the respective field in the same disc with a ‘mathematical’ crack (zero distance between lips), which is the configuration adopted in case the fracture toughness of brittle materials is determined according to the standardized cracked Brazilian-disc test. The solution is obtained using Muskhelishvili’s complex potentials’ technique adopting a suitable conformal mapping function found, also, in Savin’s milestone book. For the task to be accomplished, an auxiliary problem is first solved, namely, the infinite plate with a rectangular slit (in case the resultant force on the slit is zero and also the stresses and rotations at infinity are zero), by mapping conformally the area outside the slit onto the mathematical plane with a unit hole. The formulae obtained for the complex potentials permit the analytic exploration of the stress field along some loci of crucial practical importance. The influence of the slit’s width on the local stress amplification and also on the stress concentration around the crown of the slit is quantitatively described. In addition, the role of the load-

application mode (compression along the slit’s longitudinal symmetry axis and tension normal to it) is explored. Results indicate that the two configurations are not equivalent in terms of the stress concentration factor. In addition, depending on the combination of the slit’s width and the load-application mode, the point where the normal stress along the slit’s boundary is maximized ‘oscillates’ between the central point of the slit’s short edge (intersection of the slit’s longitudinal axis with its perimeter) and the slit’s corners.

Keywords Circular disc · Rectangular slit · Stress concentration · Fracture toughness · Stress intensity factors (SIFs) · Crack · Linear elasticity · Complex potentials

1 Introduction

Fracture toughness is a material property quantifying the resistance against initiation and further propagation of pre-existing faults resembling ‘mathematical’ cracks. The term ‘mathematical’ crack is used to denote discontinuities for which the distance between their lips approaches zero. The Mode-I fracture toughness, K_{IC} , (i.e., resistance against initiation of crack by loads normal to the crack) is an extremely useful parameter in quite a few practical applications. As a result, its laboratory determination is already standardized (ASTM 2014; ISRM 1988, 1995). Especially for brittle rock-like materials, three standardized tests are used, i.e., the “Short Rod” (SR), the “Chevron Bend” (CB) and the “Cracked Chevron Notched Brazilian Disc (CCNBD)” tests (ISRM 1988).

CCNBD was introduced by the International Society for Rock Mechanics (ISRM) to simplify the respective experimental procedure. It is “... an ideal specimen... for

✉ S. K. Kourkoulis
stakkour@central.ntua.gr

¹ Department of Mechanics, School of Applied Mathematical and Physical Sciences, National Technical University of Athens, 5 Heroes of Polytechnion Avenue, Theocaris Bld., Zografou Campus, 157 73 Athens, Greece

rock fracture toughness measurements” characterized by “... high failure load, simple loading fixture, convenient and flexible specimen preparation” (Fowell and Xu 1993). CCNBD is also extensively used to investigate mixed-mode fracture problems, since any combination of Mode-I and -II loading schemes can be achieved by properly orienting the crack with respect to the load axis.

Since its standardization in 1995, the CCNBD test is under intensive study. Quite a few papers have been published enlightening critical aspects of the experimental procedure and also of the theoretical analysis employed to calculate K_{IC} from the test’s raw data. Even today, however, 20 years after the test was standardized, some critical questions are still open: For example, a unique relationship between the K_{IC} values obtained using CCNBD specimens and differently shaped (yet standardized) ones does not as yet exist; the values obtained for the specific quantity stand well apart from each other (Erarslan 2013). It is mentioned for example that a few years ago Iqbal and Mohanty (2006, 2007) (motivated by the differences in the K_{IC} values as determined using different types of specimens) claimed that an error exists in the ISRM formula for K_{IC} . Although this suggestion was definitely anticipated by Wang et al. (2012) (who stated that such a correction “...is equivalent to replacing the original inaccurate formula with an unreasonable formula the latter being even worse because of the violation of the upper bound”), the specific point is a clear indication that additional research is required before the topic is considered as definitely closed. In this direction, Wang’s scientific group contributes for over a decade in an attempt to improve the ISRM’s formula (Wang 2010; Wang et al. 2004a, b) and the respective experimental procedure (Wang and Xing 1999; Wang et al. 2004a, b). Among others, they gave out “...a warning that the formula of ISRM was inadequate and inaccurate” (Wang et al. 2012) while recently they arrived to conclusions about the need to recalibrate the method (Wang et al. 2013). Moreover, they attempted to improve the formula taking into account three-dimensional Stress Intensity Factors (SIFs) as obtained from finite element analyses, a topic that has been studied also by Lin et al. (2015).

Along the same lines, Fowell et al. (2006) indicated that “it may be necessary to revise the dimensionless SIF values for a future release of the suggested method to incorporate some recent developments ...”. They pointed out, also, that “...more research and input from different sources need to be coordinated”. Their suggestions again reflect the fact that, despite the almost general acceptance and wide use of the CCNBD test, the topic is still open.

In our opinion, the most crucial open aspects are related to the exact formulae of the SIFs, the exact shape of the crack machined and also to the actual boundary conditions prevailing along the disc–jaw contact arc. Indeed, the

dimensionless formulae for the SIFs used in the CCNBD test are obtained from the respective “Cracked Straight Through Brazilian Disc” (CSTBD) configuration adopting either the technique proposed by Munz et al. (1980) or the respective one suggested by Bluhm (1975). Both techniques consider a finite disc with a central ‘mathematical’ crack loaded by a pair of diametral point forces. It is known, however, that in practical application both assumptions are strongly violated. The cracks machined approach rectangular slits rather than ‘mathematical’ cracks while on the other hand the disc is loaded by a complicated distribution of radial (and shear) stresses which are responsible for the generation of stress and displacement fields that only roughly correspond to the respective ones generated by a pair of point forces. The latter becomes even more crucial considering that for practical reasons the “cracks” machined cannot be very “short” (Dong 2008) and, therefore, the common assumption that the boundary conditions do not seriously influence the fields in the immediate vicinity of the crack tips is not well justified.

Besides the above practical difficulties, ‘mathematical’ cracks induce complications, also in theoretical analyses, since for specific configurations (combinations of load level and inclination of the crack with respect to the load axis) the crack lips come in contact generating contact stresses, which violate the stress-free crack lips boundary condition. This was long ago observed among others by Burniston (1969), Tweed (1970) and Pazis et al. (1988) for cracks in infinite plates and also by Atkinson et al. (1982) in their pioneering work for the finite centrally cracked disc. Atkinson et al. (1982) considered thoroughly the geometries leading to crack closure and under specific assumptions they quantified the stresses developed during the crack lips’ contact. Similar conclusions were recently drawn by Markides et al. (2011) for a ‘mathematically’ cracked disc under uniformly distributed radial stresses.

In this context, an attempt is here described to deal with some of these open questions by introducing an analytic solution for the stress field in a centrally “cracked” circular disc, assuming that the crack is not a ‘mathematical’ one but rather it resembles a rectangular slit with slightly rounded corners. Such a configuration approaches reality in a more satisfactory manner. The loading scheme considered is also closer to the actual stress distribution along the disc–jaw contact region, since it comprises a parabolic distribution of radial stresses, acting along two finite arcs. It is recalled that the solution of the respective disc–jaw contact problem (Timoshenko and Goodier 1970; Kourkoulis et al. 2012) indicates that the specific distribution is actually cyclic, however, it is excellently approximated by the parabolic one (Markides and Kourkoulis 2012) considered in the present study.

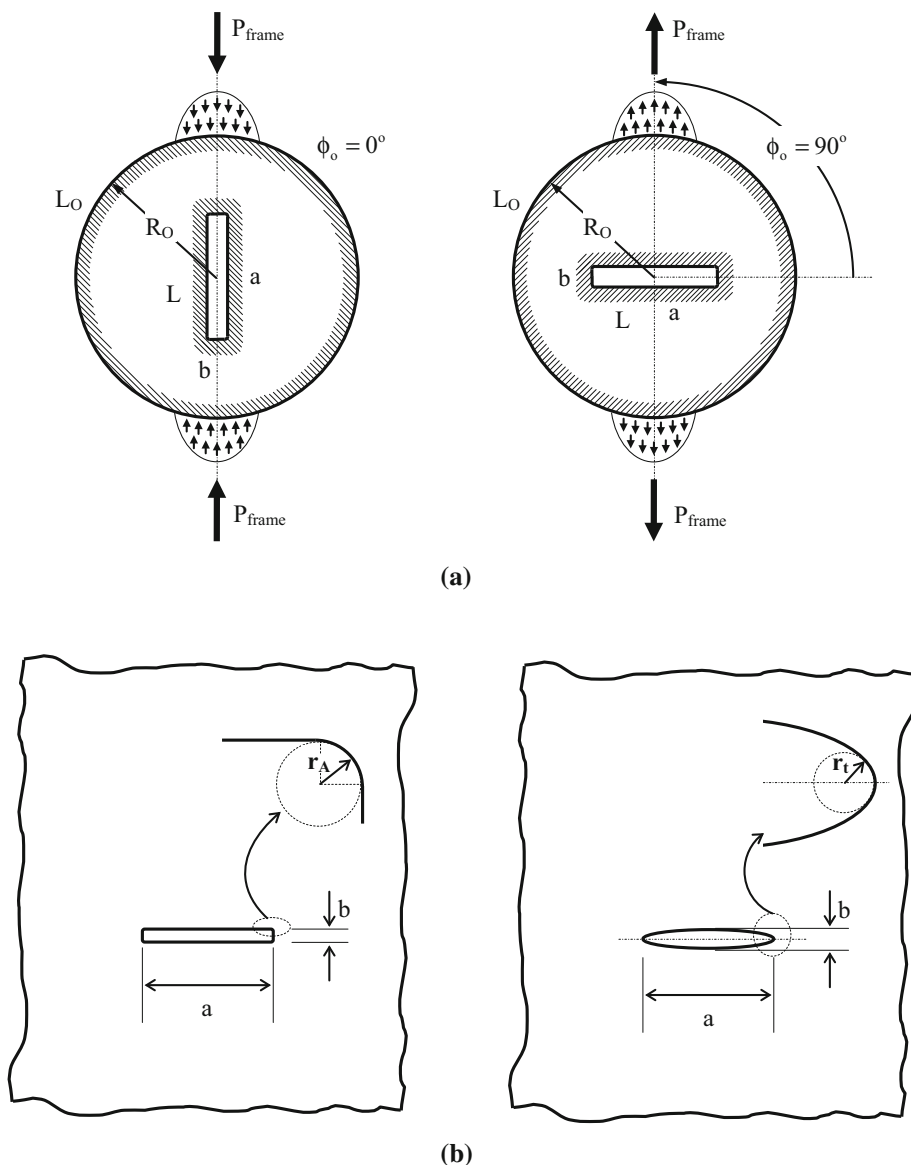
The analysis is carried out using Kolosov (1935) and Muskhelishvili (1963) complex potentials technique. Advantage is taken of recently introduced solutions for the finite ring (Kourkoulis et al. 2015a) and the finite disc with a central elliptical hole (Markides and Kourkoulis 2014a, b). Compact (though lengthy) expressions for the complex potentials characterizing the equilibrium of the disc with a rectangular slit of rounded corners are provided. Taking advantage of these expressions, the stress field is obtained along strategic loci permitting quantification of the stress concentration around the slit's corners as a function of its width. Moreover, two particular configurations which are considered equivalent to each other (disc with a central slit either under compression along the slit's axis or under tension normal to the slit's axis, Fig. 1a) are studied in juxtaposition. It is revealed that ignoring the actual features

of the configuration can lead to erroneous results especially in case of rocks for which the "cracks" machined (usually by rotating cutting discs) are neither 'mathematical' cracks nor even narrow slits.

2 'Mathematical' Cracks vs. Artificial Slits: A Short Survey

To simulate cracked bodies and quantify the respective stress fields, scientists, working experimentally, usually machine artificial slits instead of 'mathematical' cracks. This is due to practical difficulties in preparing 'mathematical' cracks, especially in case the orientation of the crack axis has to be predefined. Unfortunately, the slits machined artificially are rectangular holes with a finite

Fig. 1 a The circular disc with a rectangular slit under compression along the slit's longitudinal axis of symmetry (left) and under tension normal to the slits longitudinal axis of symmetry (right). **b** Detailed view of the actual configuration in case a slit is mechanically machined by means of a rotating disc (left) and detailed view of an elliptically shaped slit (right)



ratio a/b of their edges and also with a finite radius of curvature r_A at their corners (Fig. 1b), which is assumed to be very small compared to both a and b . On the contrary, scientists, working analytically, simulate cracks as mathematical discontinuities considering that the distance between their lips and the radius of curvature at their tips (which becomes a single point) are zero. The lips of ‘mathematical’ cracks are separated from each other exclusively by some kind of failure mechanism (for example cleavage or slip deformation) (Theocaris and Petrou 1989); no material is missing between them. In fact, the lips are in mutual contact, which generates additional difficulties in case of any loading type other than tension normal to the crack. On the other hand, for artificially machined slits an amount of material is removed and their lips are at a finite distance b apart from each other.

This inconsistency between experimental practice and theoretical simulations is the origin of quite a few problems. The most crucial one is the arbitrary transition from the “Stress Concentration” concept to the “Stress Intensity” one, as it was emphatically highlighted by Theocaris and Petrou (1989) who mentioned that: “... whereas for a real crack in an infinite... plate, the order of singularity at the tip is $\lambda = 1/2$, in the artificial crack we have a pair of corners for each tip...” creating “... a doublet of singularities for either corner, which,... are of an order depending on the angle... and the material properties... This difference in the arrangement of singularities... is of primordial interest”.

An early attempt to bridge this gap was proposed by Creager and Paris (1967) who simulated the internal cracks by ellipses with a finite radius of curvature, r_t , at their tips (Fig. 1b) assuming also that the singular points lie on the ellipse’s major semi-axis at a distance equal to $r_t/2$ from the tip of the ellipse. Under these assumptions, they provided the stress field components in the immediate vicinity of the tip by properly modifying the respective expressions for the ‘mathematical’ crack through a term depending on r_t .

An interesting approach to the problem was presented by Sinclair and Kondo (1984) who studied the stress concentration around sharp corners in two-dimensional plates. Based on energy arguments, they criticized the concept of the SIF in case it is used to describe stress fields around notches. Their main argument is that “... though SIFs can be sensibly defined for sharp notches other than cracks and could conceivably serve as a basis for engineering analyses, the usual energy argument underlying their use for cracks no longer appears to exist and the physical underpinnings of such an approach are in question”.

Later on, ‘mathematical’ cracks and artificial slits were studied in juxtaposition by Theocaris and Petrou (1987, 1988) and Theocaris (1991). They quantified the differences between the two configurations analytically and also experimentally by employing the method of caustics. They

concluded that “... the use of artificial cracks in experiments for the study of natural cracks presents several and important discrepancies concerning the stress and strain fields of the cracked plate for high levels of loading of the plate”.

The common characteristic of the studies mentioned up to this point is that they are restricted to infinite bodies. The problem is by far more complicated in case finite domains are studied. A typical example is the CSTBD configuration which is the basis for the determination of the SIFs used in the CCNBD test. According to our best knowledge, all existing solutions (Atkinson et al. 1982; Rooke and Tweed 1973; Awaji and Sato 1978) for the CSTBD configuration are based on the concept of a ‘mathematical’ crack, i.e., the circular disc is assumed as centrally cracked with a crack of zero distance between its lips and zero curvature at its tips. Possible implications due to machining rectangular slits rather than preparing ‘mathematical’ cracks were discussed by Shetty et al. (1987) well before the CCNBD geometry was standardized by ISRM. They stated that “... in polycrystalline ceramics, particularly in fine-grained ceramics, apparent fracture toughness measured with notches of finite radius tends to overestimate the true fracture toughness”.

An effort to quantify the role of the non-zero slit’s width on the fracture of chevron-notched specimens was reported by Kolhe et al. (1998). Although three-point bend chevron-notched specimens were considered, the conclusions drawn are at least indicative also for the CCNBD specimens. Kolhe et al. definitely stated that “... when the notch is wide enough the SIF vs. crack length ... no longer has a clear minimum as it does for a zero notch width sample”. Since this minimum is of crucial importance in the analysis of the test’s results, they concluded that “... this analysis clearly will not work when a minimum in $Y(\alpha)$ does not exist”. To overcome this difficulty they proposed a certain range of the relative width of the notch to ensure that a minimum of the normalized stress intensity factor $Y(\alpha)$ does exist.

Recently, Carolan et al. (2011) discussed quantitatively the role of the notch root curvature on the fracture toughness of polycrystalline cubic boron nitride and proposed specific limits beyond which the results obtained for fracture toughness are not reliable.

Taking now into account the previous discussion, it appears quite necessary to explore the possible influence of the actual shape and size of the “crack” on the results obtained from the standardized CCNBD test. This task is of course very ambitious and necessitates combined action of working groups of established international scientific associations (like ISRM or ASTM) rather than of independent researchers. In this context, the present study, devoted to the analytic derivation of the stress field in a finite circular disc with a rectangular slit (instead of a natural crack) under parabolic radial pressure, should be

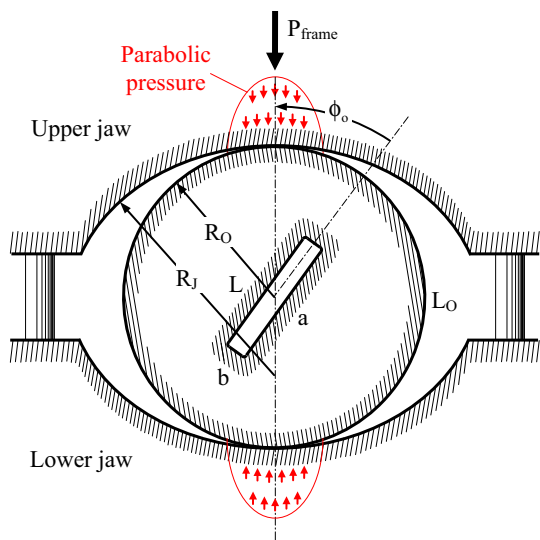


Fig. 2 A circular disc with a *rectangular slit* compressed between the jaws of the ISRM device for the standardized implementation of the Brazilian-disc test

only considered as a first step rather than as a concluding contribution.

3 Theoretical Considerations: The Complex Potentials

3.1 Formulation of the Mathematical Problem

A circular disc (radius R_O , thickness w) with a central rectangular slit L (length a , width b and slightly rounded corners) is compressed between the jaws of the device

P_{frame} and, in a first approximation, is considered as resulting to a parabolically varying distribution of radial stresses (Markides and Kourkoulis 2012) along two finite arcs of the outer boundary L_O , anti-symmetric with respect to the disc's center. The boundary L of the slit is free from stresses. In general, the axis of the slit L forms an arbitrary angle ϕ_o with respect to the axis of P_{frame} .

The problem to be solved here is the determination of the stress field developed all over the disc. The solution of this first fundamental problem is here achieved within the frame of classical plane linear elasticity. The main difficulties confronted are related to the finite dimensions of the disc as well to the fact that the length of the slit is comparable to the disc's radius. The material of the disc is assumed homogeneous and isotropic and Muskhelishvili's complex potentials technique is adopted (Muskhelishvili 1963). To solve the present problem of the disc with the rectangular slit, advantage is taken of a recently introduced solution for a circular ring of radii R_O and R_J (outer and inner, respectively) under the same as previous overall load P_{frame} . The ring was considered to be under parabolic pressure $\sigma_r = -P(\phi)$ (statically equivalent to P_{frame}), along two finite arcs (t_1t_2 and t_3t_4) of its outer periphery (Kourkoulis et al. 2015a); the length of each arc equals $2R_O\omega_o$ (Fig. 3a, before introducing the rectangular slit L). The cross section of the ring is considered in the $z = x + iy = re^{i\phi}$ complex plane and its geometric center is the origin of the Cartesian reference. The loading axis forms an arbitrary angle ϕ_o with x -axis. In this case, the complex potentials characterizing the equilibrium of the circular ring were obtained as (Kourkoulis et al. 2015a; Markides and Kourkoulis 2014a, b):

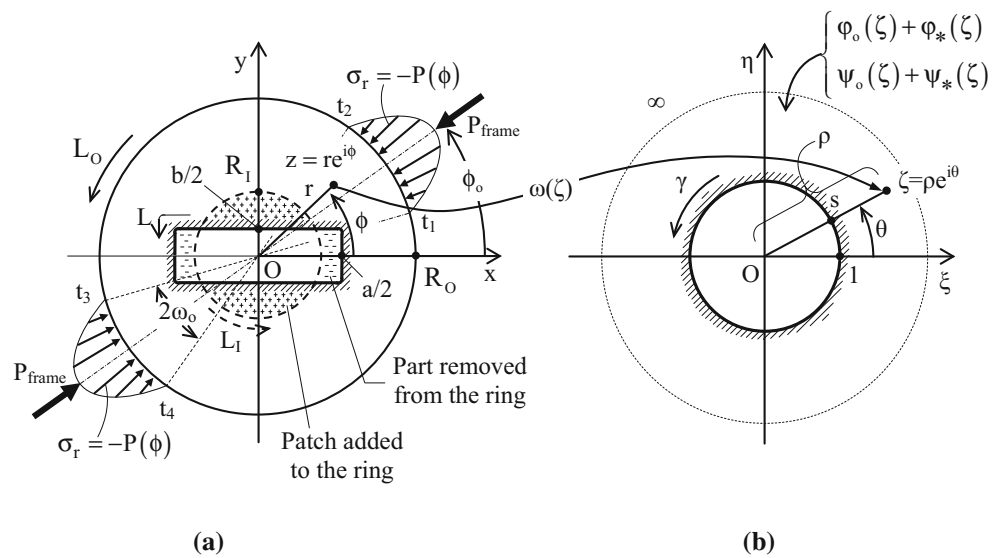
$$\varphi_o(z) = \frac{P_c}{\pi} \left\{ b_0z + \frac{B_2}{3}z^3 - B_{-2}z^{-1} + \sum_{n=1}^{\infty} \left[\frac{B_{4n}}{4n+1}z^{4n+1} - \frac{B_{-4n}}{4n-1}z^{-(4n-1)} + \frac{B_{2(2n+1)}}{4n+3}z^{4n+3} - \frac{B_{-2(2n+1)}}{4n+1}z^{-(4n+1)} \right] \right\} \tag{1}$$

$$\psi_o(z) = \frac{P_c}{\pi} \left\{ B'_0z + \frac{B'_2}{3}z^3 - b'_{-2}z^{-1} - \frac{B'_{-4}}{3}z^{-3} + \sum_{n=1}^{\infty} \left[\frac{B'_{4n}}{4n+1}z^{4n+1} + \frac{B'_{2(2n+1)}}{4n+3}z^{4n+3} - \frac{B'_{-4(n+1)}}{4n+3}z^{-(4n+3)} - \frac{B'_{-2(2n+1)}}{4n+1}z^{-(4n+1)} \right] \right\} \tag{2}$$

suggested by ISRM for the standardized implementation of the Brazilian-disc test (ISRM 1978) (Fig. 2). The radius of curvature of the jaws is $R_J = 1.5R_O$. The overall load compressing the jaws against the specimen is denoted as

The quantity P_c , which is the maximum value of $P(\phi)$, as well as the complex constants b_0 , b'_{-2} , B_j and B'_j , appearing in Eqs. (1) and (2) are analytically defined by Markides and Kourkoulis (2014a, b).

Fig. 3 a The transition from the circular ring under parabolically varying radial pressure to the circular disc with a central rectangular slit under the same loading scheme. **b** The conformal mapping



By removing parts and/or adding patches to the above ring, its circular hole L_I is transformed to the rectangular slit L as it is shown in Fig. 3a. Clearly, the presence of L , instead of L_I , will induce a disturbance in the ring’s solution. To properly cope with this problem, the complex potentials $\varphi(z)$ and $\psi(z)$ characterizing the disc with a slit are written in terms of $\varphi_o(z)$ and $\psi_o(z)$ (the respective potentials of the ring) as follows:

$$\varphi(z) = \varphi_o(z) + \varphi_*(z); \quad \psi(z) = \psi_o(z) + \psi_*(z) \quad (3)$$

where $\varphi_*(z)$ and $\psi_*(z)$ are analytic functions (to be determined) appearing exactly due to the disturbance caused by the transformation of the ring’s hole to the disc’s slit. When R_O tends to infinity, both $\varphi_*(z)$ and $\psi_*(z)$ tend to zero.

It could be anticipated at this point that the presence of a slit instead of a circular hole will somehow distort the symmetry of the distribution of $P(\phi)$ or even more that normal stresses alone are not enough to describe the actual boundary conditions. As it was analytically discussed by Markides and Kourkoulis (2014a, b, 2015a) these aspects are, in general, of minor importance for practical applications. Especially in the symmetric case with $\phi_o = 0^\circ$, which is of major interest in the present study, this distortion is definitely eliminated completely while a single pressure is enough to suffice the required global equilibrium of the disc.

3.2 Transition from the Circular Ring to the Finite Circular Disc with a Central Rectangular Slit

Transitioning from the circular ring to the disc with a rectangular slit is achieved by considering an imaginary rectangle L at the center of the ring, Fig. 3a. The area outside L is then mapped conformally on the area outside the unit circle γ (in the mathematical plane $\zeta = \xi + i\eta = \rho e^{i\theta}$, Fig. 3b) while, in addition, it is demanded that L is free from stresses. In Fig. 3b, $s = e^{i\theta}$ denotes the point ζ (for $\rho = 1$) on γ . The mapping function used in this case reads as:

$$z = \omega(\zeta) = R \left(\zeta + \sum_{\ell=1}^{\infty} \frac{c_\ell}{\zeta^{2\ell-1}} \right) \quad (4)$$

where

$$R = \frac{b}{2} \left[1 + \sum_{\ell=1}^{\infty} (-1)^\ell c_\ell \right]^{-1} \quad (5)$$

The procedure to obtain Eq. (4) (based on the well-known Schwarz–Christoffel integral formula), follows Savin (1970) work. In the same work the expressions for c_ℓ , $\ell = 1, 2, \dots, 6$, appearing in Eq. (4), can be found as:

$$\begin{aligned}
 c_1 &= \frac{\beta + \bar{\beta}}{2}; & c_2 &= \frac{(\beta - \bar{\beta})^2}{24}; & c_3 &= \frac{(\beta^2 - \bar{\beta}^2)(\beta - \bar{\beta})}{80}; \\
 c_4 &= \frac{5(\beta^4 + \bar{\beta}^4) - 4(\beta^2 + \bar{\beta}^2) - 2}{896}; \\
 c_5 &= \frac{7(\beta^5 + \bar{\beta}^5) - 5(\beta^3 + \bar{\beta}^3) - 2(\beta + \bar{\beta})}{2304}; \\
 c_6 &= \frac{21(\beta^6 + \bar{\beta}^6) - 14(\beta^4 + \bar{\beta}^4) - 5(\beta^2 + \bar{\beta}^2) - 4}{11264}
 \end{aligned}
 \tag{6}$$

In Eq. (6) it holds that $\beta = e^{i2k\pi}$, where k defines the location of the images of corner points A_1, A_2, A_3, A_4 , of L , on γ as follows (Fig. 4): $\alpha_1 = e^{ik\pi}, \alpha_2 = -e^{-ik\pi}, \alpha_3 = -e^{ik\pi}$ and $\alpha_4 = e^{-ik\pi}$, respectively; overbar denotes the complex conjugate value. As k tends to zero, b tends to zero, also, and this is the case L approaches a mathematical crack. In fact, Eq. (4) provides a quadrilateral (a, b) with rounded corners $A_j, j = 1, 2, 3, 4$ (rather than a mathematical rectangle), the radius of curvature r_A of which (Fig. 4) is given by Savin (1970) as:

$$r_A = \left[\left(\frac{\partial x(\rho, \theta)}{\partial \theta} \right)^2 + \left(\frac{\partial y(\rho, \theta)}{\partial \theta} \right)^2 \right]^{3/2} \bigg/ \left| \frac{\partial x}{\partial \theta} \frac{\partial^2 y}{\partial \theta^2} - \frac{\partial^2 x}{\partial \theta^2} \frac{\partial y}{\partial \theta} \right|
 \tag{7}$$

Using Eq. (4), and adopting the notations $\varphi(z) = \varphi(\omega(\zeta)) = \varphi(\zeta)$ and $\psi(z) = \psi(\omega(\zeta)) = \psi(\zeta)$, Eq. (3) becomes:

$$\varphi(\zeta) = \varphi_o(\zeta) + \varphi_*(\zeta); \quad \psi(\zeta) = \psi_o(\zeta) + \psi_*(\zeta)
 \tag{8}$$

Accordingly, the boundary condition for zero stresses on L , reads on γ as (Muskhelishvili 1963):

$$\varphi(s) + \frac{\omega(s)}{\omega'(s)} \overline{\varphi'(s)} + \overline{\psi(s)} = 0
 \tag{9}$$

In Eq. (9) prime denotes the first derivative.

In this way, the problem set in Sect. 3.1 has been transferred to the mathematical ζ -plane and to the determination of the analytic functions $\varphi(\zeta)$ and $\psi(\zeta)$. Substituting Eqs. (8) into Eq. (9) yields:

$$\varphi_*(s) + \frac{\omega(s)}{\omega'(s)} \overline{\varphi'_*(s)} + \overline{\psi_*(s)} = - \underbrace{\left[\varphi_o(s) + \frac{\omega(s)}{\omega'(s)} \overline{\varphi'_o(s)} + \overline{\psi_o(s)} \right]}_{f_*(s)}
 \tag{10}$$

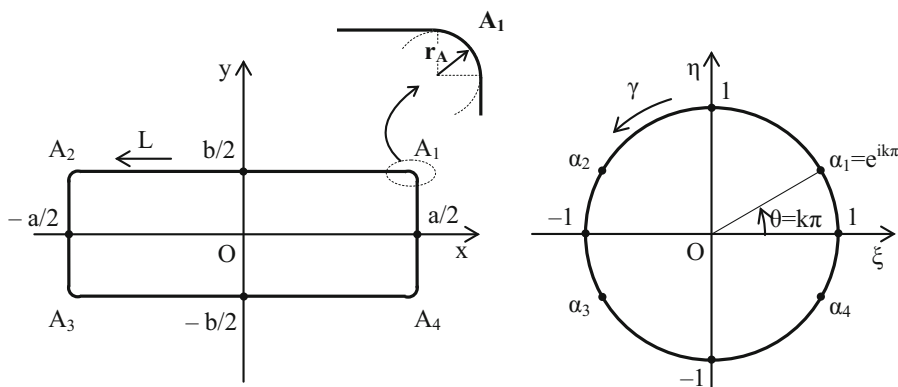
which provides $\varphi_*(\zeta)$ and $\psi_*(\zeta)$ and in turn, through Eqs. (1), (2), (4) and (8), the functions $\varphi(\zeta)$ and $\psi(\zeta)$ solving the problem.

For the solution of Eq. (10), the convenient assumption is made that the disc's radius initially tends to infinity. In this context, the problem of the infinite plate with a rectangular slit should be confronted first. To achieve this target, the general procedure outlined by Muskhelishvili (1963) for regions mapped on the inside of the unit circle with the aid of polynomials is followed. The solution of this auxiliary problem is described in Sect. 3.3.

3.3 A General Solution for the Infinite Plate with a Rectangular Slit

Consider an infinite plate with a rectangular slit L . Assume stresses are zero at infinity whereas L is subject to the most general kind of in plane external loading under the condition that the resultant vector is zero (under these assumptions displacements will turn out to be zero at infinity, too). The plate lies in the z complex plane and the origin of the coordinates is the geometric center of L . The plate's material is linearly elastic and isotropic. The problem is to find Muskhelishvili's complex potentials $\varphi_{(\infty)}(z), \psi_{(\infty)}(z)$ which characterize the plate's elastic equilibrium (subscript (∞) denotes the infinite plate).

Fig. 4 The configuration of the slit in the real plane and the respective configuration in the mathematical plane



To solve this first fundamental problem the infinite plate with the rectangular slit L is conformally mapped on the mathematical ζ -plane with the unit hole γ through the function $\omega(\zeta)$ given by Eq. (4). Writing $\varphi_{(\infty)}(z) = \varphi_{(\infty)}(\omega(\zeta)) = \varphi_{(\infty)}(\zeta)$, $\psi_{(\infty)}(z) = \psi_{(\infty)}(\omega(\zeta)) = \psi_{(\infty)}(\zeta)$, the problem reduces to the determination of the analytic functions $\varphi_{(\infty)}(\zeta)$ and $\psi_{(\infty)}(\zeta)$. To achieve that, consider the boundary condition for the stresses on L written as (Muskhelishvili 1963):

$$\varphi_{(\infty)}(s) + \frac{\omega(s)}{\omega'(s)} \overline{\varphi'_{(\infty)}(s)} + \overline{\psi_{(\infty)}(s)} = f_{(\infty)} \tag{11}$$

where $f_{(\infty)}$ is the force variation along L which is supposed to be known. In complex conjugate form Eq. (11) becomes:

$$\overline{\varphi_{(\infty)}(s)} + \frac{\overline{\omega(s)}}{\overline{\omega'(s)}} \varphi'_{(\infty)}(s) + \psi_{(\infty)}(s) = \overline{f_{(\infty)}} \tag{12}$$

According to the assumptions made in the beginning of this section, both $\varphi_{(\infty)}(\zeta)$ and $\psi_{(\infty)}(\zeta)$ will be holomorphic outside γ and vanishing at infinity. Then, multiplying Eq. (12) by $(1/2\pi i)[ds/(s - \zeta)]$, where ζ lies outside γ , and integrating along γ , one obtains $\psi_{(\infty)}(\zeta)$ as:

$$\psi_{(\infty)}(\zeta) = \frac{1}{2\pi i} \int_{\gamma} \frac{\overline{\omega(s)}}{\overline{\omega'(s)}} \varphi'_{(\infty)}(s) \frac{ds}{s - \zeta} - \frac{1}{2\pi i} \int_{\gamma} \frac{\overline{f_{(\infty)}} ds}{s - \zeta} \tag{13}$$

Similarly, Eq. (11) provides $\varphi_{(\infty)}(\zeta)$, for ζ outside γ , as:

$$\varphi_{(\infty)}(\zeta) = \frac{1}{2\pi i} \int_{\gamma} \frac{\omega(s)}{\omega'(s)} \overline{\varphi'_{(\infty)}(s)} \frac{ds}{s - \zeta} - \frac{1}{2\pi i} \int_{\gamma} \frac{f_{(\infty)} ds}{s - \zeta} \tag{14}$$

Equation (14) is the general functional equation which provides $\varphi_{(\infty)}(\zeta)$ and in turn $\psi_{(\infty)}(\zeta)$ through Eq. (13), i.e., the general solution of the present problem. To solve Eq. (14) consider that $[\omega(s)/\omega'(s)] \cdot \overline{\varphi'_{(\infty)}(s)}$ is the boundary value of the function $[\omega(\zeta)/\omega'(\frac{1}{\zeta})] \cdot \overline{\varphi'_{(\infty)}(\frac{1}{\zeta})}$, which is holomorphic inside γ , except at $\zeta = 0$, where it has a pole of n th order. Since $\varphi_{(\infty)}(\zeta)$ is holomorphic outside γ and vanishes at infinity, it can be written that:

$$\varphi_{(\infty)}(\zeta) = \frac{d_1^{(\infty)}}{\zeta} + \frac{d_2^{(\infty)}}{\zeta^2} + \dots \tag{15}$$

whence

$$\overline{\varphi'_{(\infty)}\left(\frac{1}{\zeta}\right)} = -\overline{d_1^{(\infty)}}\zeta^2 - 2\overline{d_2^{(\infty)}}\zeta^3 - \dots \quad \text{for } |\zeta| < 1 \tag{16}$$

Considering only the first six additional terms of $\omega(\zeta)$ in Eq. (4), it can be written that:

$$\omega(\zeta) / \overline{\omega'\left(\frac{1}{\zeta}\right)} = \frac{c_1}{\zeta} + \frac{c_2}{\zeta^3} + \dots + \frac{c_6}{\zeta^{11}} + F(\zeta) \tag{17}$$

where $F(\zeta)$ is holomorphic inside γ . Combining Eqs. (16) and (17) it follows that:

$$\left[\omega(\zeta) / \overline{\omega'\left(\frac{1}{\zeta}\right)} \right] \cdot \overline{\varphi'_{(\infty)}\left(\frac{1}{\zeta}\right)} = \frac{K_1^{(\infty)}}{\zeta} + \frac{K_2^{(\infty)}}{\zeta^2} + \dots + \frac{K_9^{(\infty)}}{\zeta^9} + Q(\zeta) \tag{18}$$

with $Q(\zeta)$ a function holomorphic inside γ . $K_j^{(\infty)}$ are expressed as:

$$\begin{aligned} K_1^{(\infty)} &= -(\overline{d_1^{(\infty)}}c_2 + 3\overline{d_3^{(\infty)}}c_3 + 5\overline{d_5^{(\infty)}}c_4 + 7\overline{d_7^{(\infty)}}c_5 + 9\overline{d_9^{(\infty)}}c_6); \\ K_2^{(\infty)} &= -(\overline{2d_2^{(\infty)}}c_3 + 4\overline{d_4^{(\infty)}}c_4 + 6\overline{d_6^{(\infty)}}c_5 + 8\overline{d_8^{(\infty)}}c_6); \\ K_3^{(\infty)} &= -(\overline{d_1^{(\infty)}}c_3 + 3\overline{d_3^{(\infty)}}c_4 + 5\overline{d_5^{(\infty)}}c_5 + 7\overline{d_7^{(\infty)}}c_6); \\ K_4^{(\infty)} &= -(\overline{2d_2^{(\infty)}}c_4 + 4\overline{d_4^{(\infty)}}c_5 + 6\overline{d_6^{(\infty)}}c_6); \\ K_5^{(\infty)} &= -(\overline{d_1^{(\infty)}}c_4 + 3\overline{d_3^{(\infty)}}c_5 + 5\overline{d_5^{(\infty)}}c_6); \\ K_6^{(\infty)} &= -(\overline{2d_2^{(\infty)}}c_5 + 4\overline{d_4^{(\infty)}}c_6); \\ K_7^{(\infty)} &= -(\overline{d_1^{(\infty)}}c_5 + 3\overline{d_3^{(\infty)}}c_6); \\ K_8^{(\infty)} &= -\overline{2d_2^{(\infty)}}c_6; \quad K_9^{(\infty)} = -\overline{d_1^{(\infty)}}c_6 \end{aligned} \tag{19}$$

Then, using a well-known property of Cauchy-type integrals, it is obtained that:

$$\frac{1}{2\pi i} \int_{\gamma} \frac{\omega(s)}{\omega'(s)} \overline{\varphi'_{(\infty)}(s)} \frac{ds}{s - \zeta} = -\frac{K_1^{(\infty)}}{\zeta} - \frac{K_2^{(\infty)}}{\zeta^2} - \dots - \frac{K_9^{(\infty)}}{\zeta^9} \tag{20}$$

Substituting from Eq. (20) into Eq. (14), $\varphi_{(\infty)}(\zeta)$ is obtained as:

$$\varphi_{(\infty)}(\zeta) = -\frac{1}{2\pi i} \int_{\gamma} \frac{f_{(\infty)} ds}{s - \zeta} - \frac{K_1^{(\infty)}}{\zeta} - \frac{K_2^{(\infty)}}{\zeta^2} - \dots - \frac{K_9^{(\infty)}}{\zeta^9} \tag{21}$$

Similarly, Eq. (13) yields:

$$\begin{aligned} \psi_{(\infty)}(\zeta) &= -\frac{1}{2\pi i} \int_{\gamma} \frac{\overline{f_{(\infty)}} ds}{s - \zeta} - \overline{\omega\left(\frac{1}{\zeta}\right)} \frac{\varphi'_{(\infty)}(\zeta)}{\omega'(\zeta)} + \overline{K_1^{(\infty)}}\zeta \\ &\quad + \overline{K_2^{(\infty)}}\zeta^2 + \dots + \overline{K_9^{(\infty)}}\zeta^9 \end{aligned} \tag{22}$$

with $\varphi_{(\infty)}(\zeta)$ given by Eq. (21). Concerning $K_j^{(\infty)}$, appearing in the general solution (Eqs. 21, 22), they can be obtained according to the following procedure:

Consider that for $|s| = 1 < |\zeta|$ it holds:

$$\frac{1}{s - \zeta} = -\frac{1}{\zeta} \left(1 + \frac{s}{\zeta} + \frac{s^2}{\zeta^2} + \dots \right) \tag{23}$$

From Eq. (23) the integral on the right-hand side of Eq. (21) becomes:

$$-\frac{1}{2\pi i} \int_{\gamma} \frac{f(\infty) ds}{s - \zeta} = \sum_{j=1}^{\infty} \frac{N_j^{(\infty)}}{\zeta^j} \tag{24}$$

with $N_j^{(\infty)} = \frac{1}{2\pi i} \int_{\gamma} f(\infty) s^{j-1} ds$. Then substituting from Eqs. (15), (19) and (24) into Eq. (21) and comparing terms of ζ of the same order up to $(1/\zeta^9)$, the following system of nine linear equations is obtained, which provides the real and imaginary parts of $d_j^{(\infty)}$:

$$\begin{aligned} d_1^{(\infty)} - \overline{d_1^{(\infty)}} c_2 - 3\overline{d_3^{(\infty)}} c_3 - 5\overline{d_5^{(\infty)}} c_4 - 7\overline{d_7^{(\infty)}} c_5 \\ - 9\overline{d_9^{(\infty)}} c_6 = N_1^{(\infty)}; \\ d_2^{(\infty)} - 2\overline{d_2^{(\infty)}} c_3 - 4\overline{d_4^{(\infty)}} c_4 - 6\overline{d_6^{(\infty)}} c_5 - 8\overline{d_8^{(\infty)}} c_6 = N_2^{(\infty)}; \\ d_3^{(\infty)} - \overline{d_1^{(\infty)}} c_3 - 3\overline{d_3^{(\infty)}} c_4 - 5\overline{d_5^{(\infty)}} c_5 - 7\overline{d_7^{(\infty)}} c_6 = N_3^{(\infty)}; \\ d_4^{(\infty)} - 2\overline{d_2^{(\infty)}} c_4 - 4\overline{d_4^{(\infty)}} c_5 - 6\overline{d_6^{(\infty)}} c_6 = N_4^{(\infty)}; \\ d_5^{(\infty)} - \overline{d_1^{(\infty)}} c_4 - 3\overline{d_3^{(\infty)}} c_5 - 5\overline{d_5^{(\infty)}} c_6 = N_5^{(\infty)}; \\ d_6^{(\infty)} - 2\overline{d_2^{(\infty)}} c_5 - 4\overline{d_4^{(\infty)}} c_6 = N_6^{(\infty)}; \\ d_7^{(\infty)} - \overline{d_1^{(\infty)}} c_5 - 3\overline{d_3^{(\infty)}} c_6 = N_7^{(\infty)}; d_8^{(\infty)} - 2\overline{d_2^{(\infty)}} \\ c_6 = N_8^{(\infty)}; d_9^{(\infty)} - \overline{d_1^{(\infty)}} c_6 = N_9^{(\infty)} \end{aligned} \tag{25}$$

Once $d_j^{(\infty)}$ have been found, $K_j^{(\infty)}$ are directly obtained by Eqs. (19).

3.4 The Complex Potentials for the Circular Disc with the Rectangular Slit

To return to the finite circular disc with the rectangular slit, assume instantly, that its radius tends to infinity. Then, according to the general solution of the infinite plate with the rectangular slit (obtained in previous Sect. 3.3), $\varphi_*(\zeta)$ and $\psi_*(\zeta)$ appearing in Eq. (10) will be of the form:

$$\varphi_*(\zeta) = -\frac{1}{2\pi i} \int_{\gamma} \frac{f_* ds}{s - \zeta} - \frac{K_1^*}{\zeta} - \frac{K_2^*}{\zeta^2} - \dots - \frac{K_9^*}{\zeta^9} \tag{26}$$

$$\psi_*(\zeta) = -\frac{1}{2\pi i} \int_{\gamma} \frac{\overline{f_*} ds}{s - \zeta} - \overline{c} \left(\frac{1}{\zeta} \right) \frac{\varphi'_*(\zeta)}{c \varphi'(\zeta)} + \overline{K_1^*} \zeta + \overline{K_2^*} \zeta^2 + \dots + \overline{K_9^*} \zeta^9 \tag{27}$$

In Eqs. (26) and (27) K_j^* satisfy formally expressions exactly similar to those of Eq. (19), which are not repeated here for obvious brevity reasons. The only difference is that $d_j^{(\infty)}$ are now replaced by d_j^* (i.e. the coefficients of $\varphi_*(\zeta)$) which are provided by a system of equations exactly similar to that of Eqs. (25). Along the same lines, $N_j^{(\infty)}$, appearing in Eqs. (25), must be substituted by N_j^* (which are obtained from Eq. (24), after simply replacing $f(\infty)$ by f_*).

Performing the above-mentioned substitutions in Eqs. (26), (27) and then introducing them into Eqs. (8), the solution of the problem is finally achieved as:

$$\begin{aligned} \varphi(\zeta) = \frac{Pc}{\pi} \left\{ b_0 R \left(\zeta - \frac{c_1}{\zeta} - \frac{c_2}{\zeta^3} - \frac{c_3}{\zeta^5} - \frac{c_4}{\zeta^7} - \frac{c_5}{\zeta^9} - \frac{c_6}{\zeta^{11}} \right) + B_2 R^3 \zeta \left(c_1 + \frac{\zeta^2}{3} \right) - \frac{\overline{B_2} R^3}{\zeta} \left[1 + 2(c_1^2 + c_2^2 \right. \right. \\ \left. \left. + c_3^2 + c_4^2 + c_5^2 + c_6^2) + c_2(c_1^2 + c_2 c_4) + 2c_1 c_3(c_2 + c_4) + 2c_1 c_5(c_4 + c_6) + 2c_2(c_3 c_5 + c_4 c_6) + c_3^2 c_6 \right. \right. \\ \left. \left. + (c_1(1 + c_1 c_3) + 2c_1 c_2(1 + c_4) + 2c_2 c_3(1 + c_6) + 2c_3(c_4 + c_1 c_5) + c_5(c_2^2 + 2c_4 + 2c_6) + 2c_1 c_4 c_6) / \zeta^2 \right. \right. \\ \left. \left. + (c_2(1 + 2c_4) + 2c_1 c_3(1 + c_6) + c_4(c_1^2 + 2c_6) + 2c_5(c_1 c_2 + c_3) + c_2^2 c_6) / \zeta^4 + (c_3(1 + 2c_6) \right. \right. \\ \left. \left. + c_1(2c_4 + c_1 c_5) + 2c_2(c_5 + c_1 c_6)) / \zeta^6 + (c_4 + c_1(2c_5 + c_1 c_6) + 2c_2 c_6) / \zeta^8 + \frac{c_5 + 2c_1 c_6}{\zeta^{10}} + \frac{c_6}{\zeta^{12}} \right] \right. \\ \left. - \frac{\overline{B_{-2}}}{R \zeta} \left(c_2 + \frac{c_3}{\zeta^2} + \frac{c_4}{\zeta^4} + \frac{c_5}{\zeta^6} + \frac{c_6}{\zeta^8} \right) - \frac{\overline{B'_0} R}{\zeta} - \frac{\overline{B'_2} R^3}{\zeta} \left(c_1 + \frac{1}{3\zeta^2} \right) - \frac{\overline{B_{-4n}}}{R^3 \zeta} \left(c_3 + \frac{c_4}{\zeta^2} + \frac{c_5}{\zeta^4} + \frac{c_6}{\zeta^6} \right) \right|_{n=1} \\ \left. - \frac{\overline{B_{-4n}}}{R^7 \zeta} \left(c_5 + \frac{c_6}{\zeta^2} \right) \right|_{n=2} - \frac{\overline{B_{-2(2n+1)}}}{R^5 \zeta} \left(c_4 + \frac{c_5}{\zeta^2} + \frac{c_6}{\zeta^4} \right) \right|_{n=1} - \frac{\overline{B_{-2(2n+1)}}}{R^9} \frac{c_6}{\zeta} \right|_{n=2} + \sum_{n=1}^{\infty} R^{4n+1} \left[\frac{B_{4n}}{4n+1} G_{4n+1}^{(\infty)}(\zeta) \right. \\ \left. - \overline{B_{4n}} G_{4n}^{(0)}(\zeta) - \frac{\overline{B'_{4n}}}{4n+1} G_{4n+1}^{(0)}(\zeta) + R^2 \left(\frac{B_{2(2n+1)}}{4n+3} G_{4n+3}^{(\infty)}(\zeta) - \overline{B_{2(2n+1)}} G_{2(2n+1)}^{(0)}(\zeta) - \frac{B'_{2(2n+1)}}{4n+3} G_{4n+3}^{(0)}(\zeta) \right) \right] \left. \right\} \\ - \left(\frac{K_1^*}{\zeta} + \frac{K_2^*}{\zeta^2} + \frac{K_3^*}{\zeta^3} + \frac{K_4^*}{\zeta^4} + \frac{K_5^*}{\zeta^5} + \frac{K_6^*}{\zeta^6} + \frac{K_7^*}{\zeta^7} + \frac{K_8^*}{\zeta^8} + \frac{K_9^*}{\zeta^9} \right) \end{aligned} \tag{28}$$

$$\begin{aligned}
\psi(\zeta) = & \frac{P_c}{\pi} \left\{ -b_0 R \left[\frac{1}{\zeta} - c_1 \zeta - c_2 \zeta^3 - c_3 \zeta^5 - c_4 \zeta^7 - c_5 \zeta^9 - c_6 \zeta^{11} + \left(1 + \frac{c_1}{\zeta^2} + \frac{3c_2}{\zeta^4} + \frac{5c_3}{\zeta^6} + \frac{7c_4}{\zeta^8} \right. \right. \right. \\
& + \frac{9c_5}{\zeta^{10}} + \frac{11c_6}{\zeta^{12}} \left. \right] \bar{\omega} \left(\frac{1}{\zeta} \right) / \omega'(\zeta) - \frac{\bar{B}_2 R^3}{\zeta^2} \left[\zeta \left(c_1 + \frac{1}{3\zeta^2} \right) + [1 + 2(c_1^2 + c_2^2 + c_3^2 + c_4^2 + c_5^2 + c_6^2) \right. \\
& + c_2(c_1^2 + c_2c_4) + 2c_1c_3(c_2 + c_4) + 2c_1c_5(c_4 + c_6) + 2c_2(c_3c_5 + c_4c_6) + c_3^2c_6 + 3(c_1(1 + c_1c_3) \\
& + 2c_1c_2(1 + c_4) + 2c_2c_3(1 + c_6) + 2c_3(c_4 + c_1c_5) + c_5(c_2^2 + 2c_4 + 2c_6) + 2c_1c_4c_6) / \zeta^2 \\
& + 5(c_2(1 + 2c_4) + 2c_1c_3(1 + c_6) + c_4(c_1^2 + 2c_6) + 2c_5(c_1c_2 + c_3) + c_2^2c_6) / \zeta^4 + 7(c_3(1 + 2c_6) \\
& + c_1(2c_4 + c_1c_5) + 2c_2(c_5 + c_1c_6)) / \zeta^6 + 9(c_4 + c_1(2c_5 + c_1c_6) + 2c_2c_6) / \zeta^8 + 11 \frac{c_5 + 2c_1c_6}{\zeta^{10}} + 13 \frac{c_6}{\zeta^{12}} \left. \right] \\
& \cdot \bar{\omega} \left(\frac{1}{\zeta} \right) / \omega'(\zeta) + B_2 R^3 \zeta [1 + 2(c_1^2 + c_2^2 + c_3^2 + c_4^2 + c_5^2 + c_6^2) + c_2(c_1^2 + c_2c_4) + 2c_1c_3(c_2 + c_4) \\
& + 2c_1c_5(c_4 + c_6) + 2c_2(c_3c_5 + c_4c_6) + c_3^2c_6 + (c_1(1 + c_1c_3) + 2c_1c_2(1 + c_4) + 2c_2c_3(1 + c_6) \\
& + 2c_3(c_4 + c_1c_5) + c_5(c_2^2 + 2c_4 + 2c_6) + 2c_1c_4c_6) \zeta^2 + (c_2(1 + 2c_4) + 2c_1c_3(1 + c_6) + c_4(c_1^2 + 2c_6) \\
& + 2c_5(c_1c_2 + c_3) + c_2^2c_6) \zeta^4 + (c_3(1 + 2c_6) + c_1(2c_4 + c_1c_5) + 2c_2(c_5 + c_1c_6)) \zeta^6 + (c_4 + c_1(2c_5 + c_1c_6) \\
& + 2c_2c_6) \zeta^8 + (c_5 + 2c_1c_6) \zeta^{10} + c_6 \zeta^{12} - \frac{c_1 + \zeta^2}{\zeta} \bar{\omega} \left(\frac{1}{\zeta} \right) / \omega'(\zeta) \left. \right] + B'_0 R \zeta + B'_2 R^3 \zeta \left(c_1 + \frac{\zeta^2}{3} \right) + \frac{B_{-2}}{R} \zeta (c_2 + c_3 \zeta^2 \\
& + c_4 \zeta^4 + c_5 \zeta^6 + c_6 \zeta^8) + \frac{B_{-4n}}{R^3} \zeta (c_3 + c_4 \zeta^2 + c_5 \zeta^4 + c_6 \zeta^6) \Big|_{n=1} + \frac{B_{-4n}}{R^7} \zeta (c_5 + c_6 \zeta^2) \Big|_{n=2} + \frac{B_{-2(2n+1)}}{R^9} c_6 \zeta \Big|_{n=2} \\
& + \frac{B_{-2(2n+1)}}{R^5} \zeta (c_4 + c_5 \zeta^2 + c_6 \zeta^4) \Big|_{n=1} - \frac{\bar{\omega} \left(\frac{1}{\zeta} \right)}{\omega'(\zeta)} \left[\frac{\bar{B}_{-2}}{R \zeta^2} \left(c_2 + \frac{3c_3}{\zeta^2} + \frac{5c_4}{\zeta^4} + \frac{7c_5}{\zeta^6} + \frac{9c_6}{\zeta^8} \right) + \frac{\bar{B}'_0 R}{\zeta^2} + \frac{\bar{B}'_2 R^3}{\zeta^2} \left(c_1 + \frac{1}{\zeta^2} \right) \right. \\
& + \frac{\bar{B}_{-4n}}{R^3 \zeta^2} \left(c_3 + \frac{3c_4}{\zeta^2} + \frac{5c_5}{\zeta^4} + \frac{7c_6}{\zeta^6} \right) \Big|_{n=1} + \frac{\bar{B}_{-4n}}{R^7 \zeta^2} \left(c_5 + \frac{3c_6}{\zeta^2} \right) \Big|_{n=2} + \frac{\bar{B}_{-2(2n+1)}}{R^5 \zeta^2} \left(c_4 + \frac{3c_5}{\zeta^2} + \frac{5c_6}{\zeta^4} \right) \Big|_{n=1} + \frac{\bar{B}_{-2(2n+1)}}{R^9 \zeta^2} c_6 \Big|_{n=2} \left. \right] \\
& + \sum_{n=1}^{\infty} R^{4n+1} \left[-\bar{B}_{4n} \left[\frac{G_{4n+1}^{(0)}(\zeta)}{4n+1} - \frac{dG_{4n}^{(0)}(\zeta)}{d\zeta} \bar{\omega} \left(\frac{1}{\zeta} \right) / \omega'(\zeta) \right] - \bar{B}_{2(2n+1)} R^2 \left[\frac{G_{4n+3}^{(0)}(\zeta)}{4n+3} - \frac{dG_{2(2n+1)}^{(0)}(\zeta)}{d\zeta} \bar{\omega} \left(\frac{1}{\zeta} \right) / \omega'(\zeta) \right] \right. \\
& + B_{4n} \left[G_{4n}^{(\infty)}(\zeta) - \frac{1}{4n+1} \frac{dG_{4n+1}^{(\infty)}(\zeta)}{d\zeta} \bar{\omega} \left(\frac{1}{\zeta} \right) / \omega'(\zeta) \right] + B_{2(2n+1)} R^2 \left[G_{2(2n+1)}^{(\infty)}(\zeta) - \frac{1}{4n+3} \frac{dG_{4n+3}^{(\infty)}(\zeta)}{d\zeta} \bar{\omega} \left(\frac{1}{\zeta} \right) / \omega'(\zeta) \right] \\
& + \frac{B'_{4n}}{4n+1} G_{4n+1}^{(\infty)}(\zeta) + \frac{B'_{2(2n+1)}}{4n+3} R^2 G_{4n+3}^{(\infty)}(\zeta) + \left[\frac{\bar{B}'_{4n}}{4n+1} \frac{dG_{4n+1}^{(0)}(\zeta)}{d\zeta} + \frac{\bar{B}'_{2(2n+1)}}{4n+3} R^2 \frac{dG_{4n+3}^{(0)}(\zeta)}{d\zeta} \right] \bar{\omega} \left(\frac{1}{\zeta} \right) / \omega'(\zeta) \left. \right\} \\
& - \left(\frac{K_1^*}{\zeta^2} + \frac{2K_2^*}{\zeta^3} + \frac{3K_3^*}{\zeta^4} + \frac{4K_4^*}{\zeta^5} + \frac{5K_5^*}{\zeta^6} + \frac{6K_6^*}{\zeta^7} + \frac{7K_7^*}{\zeta^8} + \frac{8K_8^*}{\zeta^9} + \frac{9K_9^*}{\zeta^{10}} \right) \bar{\omega} \left(\frac{1}{\zeta} \right) / \omega'(\zeta) \\
& + \bar{K}_1^* \zeta + \bar{K}_2^* \zeta^2 + \bar{K}_3^* \zeta^3 + \bar{K}_4^* \zeta^4 + \bar{K}_5^* \zeta^5 + \bar{K}_6^* \zeta^6 + \bar{K}_7^* \zeta^7 + \bar{K}_8^* \zeta^8 + \bar{K}_9^* \zeta^9
\end{aligned}
\tag{29}$$

where

$$\bar{\omega} \left(\frac{1}{\zeta} \right) / \omega'(\zeta) = \frac{\frac{1}{\zeta} + c_1 \zeta + c_2 \zeta^3 + c_3 \zeta^5 + c_4 \zeta^7 + c_5 \zeta^9 + c_6 \zeta^{11}}{1 - \frac{c_1}{\zeta^2} - \frac{3c_2}{\zeta^4} - \frac{5c_3}{\zeta^6} - \frac{7c_4}{\zeta^8} - \frac{9c_5}{\zeta^{10}} - \frac{11c_6}{\zeta^{12}}}
\tag{30}$$

In the above formulae, $G_j^{(\infty)}(\zeta)$ and $G_j^{(0)}(\zeta)$ are principal parts of analytic functions appearing in the solution, at the points $\zeta = \infty$ and $\zeta = 0$, respectively, i.e., parts of these functions spanning poles at the respective points. Their

analytic expressions (for the first six additional terms of Eq. (4) taken into consideration here) are given, for brevity reasons, in Appendix, in the order they appear in Eqs. (28) and (29).

It is mentioned that the above formulae are also applicable in case the disc is subjected to a parabolic distribution of tensile radial stresses along the loaded rims (instead of pressure), case which will also be considered later on. For this case one must only introduce a minus sign before P_c in Eqs. (28) and (29), directly as a constant multiplier

factor, and indirectly through K_j^* (actually, via N_j^* containing P_c and in turn via d_j^* which provide K_j^*).

4 The Stress Field along Some Characteristic Loci

As a next step, advantage is taken of Muskhelishvili's (1963) well-known formulae for the stress field considered here in the convenient form:

$$\sigma_x - i\sigma_{xy} = 2\Re\Phi(\zeta) - \frac{\overline{\omega(\zeta)}}{\omega'(\zeta)} \Phi'(\zeta) - \Psi(\zeta), \tag{31}$$

$$\sigma_x + \sigma_y = 4\Re\Phi(\zeta)$$

providing the Cartesian components of the stress field at any point of the disc in terms of $\varphi(\zeta)$ and $\psi(\zeta)$ (Eqs. 28 and 29, respectively), for either compressive ($+P_c$) or tensile ($-P_c$) stresses parabolically distributed along the loaded rim. In Eq. (31) \Re is the real part while it holds that:

$$\Phi(\zeta) = \frac{\varphi'(\zeta)}{\omega'(\zeta)}, \quad \Psi(\zeta) = \frac{\psi'(\zeta)}{\omega'(\zeta)} \tag{32}$$

Alternatively, one may use the traditional formulae (Muskhelishvili 1963):

$$\sigma_\rho - i\sigma_{\rho\theta} = 2\Re\Phi(\zeta) - \frac{e^{2i\theta}}{\overline{\omega'(\zeta)}} \left[\overline{\omega(\zeta)} \Phi'(\zeta) + \omega'(\zeta) \Psi(\zeta) \right],$$

$$\sigma_\rho + \sigma_\theta = 4\Re\Phi(\zeta) \tag{33}$$

which provide the stress components at any point $z = re^{i\phi}$ of the real disc in the curvilinear coordinate system (ρ, θ) (see Fig. 5).

The explicit expressions for the stress components provided using the above formulae (Eqs. 31 and 33) are not given here since they are extremely lengthy. On the other hand, for the needs of the present paper, attention will be focused exclusively on specific loci, which are of strategic importance for practical applications of the cracked Brazilian-disc test and especially for the determination of Mode-I fracture toughness K_{IC} .

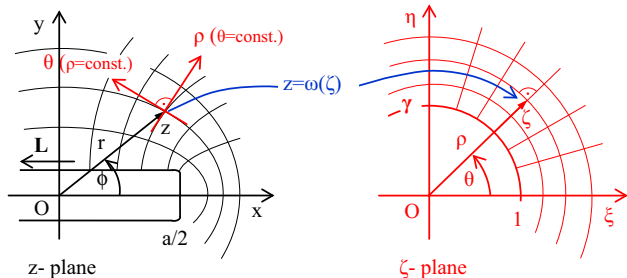


Fig. 5 The correspondence between characteristic loci and reference systems (Cartesian and curvilinear) in the real and in the mathematical planes (z - and ζ -plane, respectively)

In the context of the discussion outlined in Sect. 1, the loci of interest for the determination of the Stress Intensity (or of the respective Stress Concentration) are:

1. The axis of symmetry of the disc along the slit's longitudinal axis.
2. The perimeter L of the slit.

4.1 The Stress Field along the Longitudinal Symmetry Axis of the Slit for Compression at $\phi_o = 0^\circ$ and Tension at $\phi_o = 90^\circ$ (Mode-I Loading Conditions)

For the features of the stress field along the locus with $y = 0$ and $x \in [a/2, R_O]$ to be enlightened, two configurations are considered. A disc of radius $R_O = 50$ mm and width $w = 10$ mm with a central rectangular slit of dimensions $(a \times b) = (50 \text{ mm} \times 3 \text{ mm})$, and a second disc of the same dimensions, but with a much narrower slit with $(a \times b) = (50 \text{ mm} \times 0.6 \text{ mm})$. Both discs are loaded by the same overall load P_{frame} , which is either of compressive nature, applied parallel (i.e., $\phi_o = 0^\circ$) to the longitudinal axis of the slit, or it is of tensile nature applied normally (i.e., $\phi_o = 90^\circ$) to the longitudinal axis of the slit (Fig. 1a).

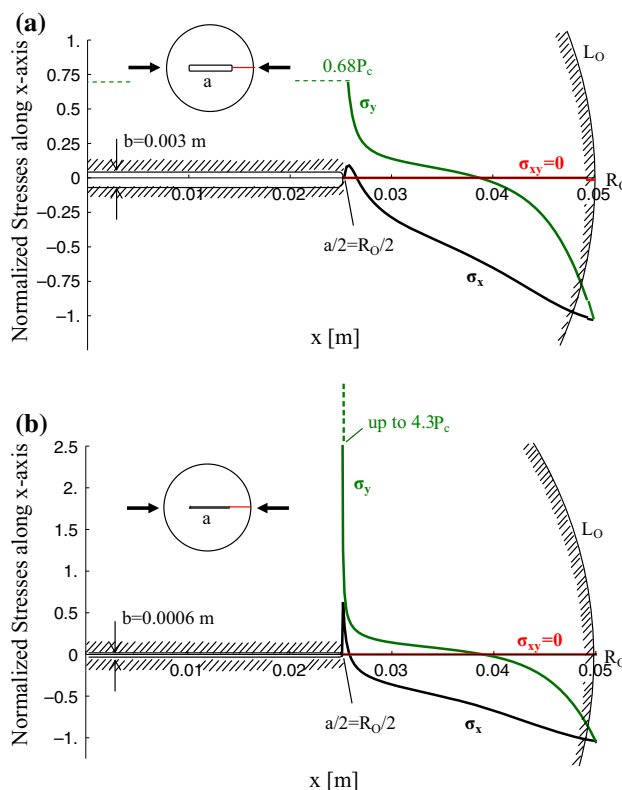


Fig. 6 The stress field along the slit's longitudinal axis of symmetry for $b = 3$ mm (a) and $b = 0.6$ mm (b) for compression parallel ($\phi_o = 0^\circ$) to the slit's longitudinal axis

For the first case (i.e., compression at $\phi_o = 0^\circ$), the stress components along the locus under study for the above two configurations ($b = 3 \text{ mm}$ and $b = 0.6 \text{ mm}$) are plotted in Fig. 6. To draw this figure, one can use either the formulae of Eqs. (31) or those of Eqs. (33) ($\sigma_x \equiv \sigma_\rho$, $\sigma_y \equiv \sigma_\theta$, $\sigma_{xy} \equiv \sigma_{\rho\theta}$), by setting $\theta = 0^\circ$. The values of the stresses are normalized against the amplitude P_c of the radial pressure applied along the loaded arcs of the disc. As it is expected, for obvious symmetry reasons, the shear stress component σ_{xy} is zero all along the specific locus. For the normal stresses σ_x and σ_y , the distributions for the two configurations (shown in Fig. 6a for $b = 3 \text{ mm}$ and in Fig. 6b for $b = 0.6 \text{ mm}$) are qualitatively similar: the longitudinal normal stress σ_x is negative almost all along the locus considered and only as $x \rightarrow a/2$ ($=R_o/2$) it becomes positive and is then suddenly zeroed as x becomes equal to $a/2$. The transverse normal stress behaves in a different manner: it is compressive from $x = R_o$ until $x \approx 0.8R_o$ and then it changes sign becoming tensile. Its magnitude keeps increasing smoothly for both configurations until $x \rightarrow a/2$ where it starts increasing abruptly. It is worth emphasizing, however, that its value *remains bounded* (i.e., its value does not tend to infinity) contrary to what happens at the tips of a ‘mathematical’ crack in the frame of linear elasticity.

From a quantitative point of view, now, things are dramatically different for the two configurations considered. For $x = R_o$ both σ_x and σ_y are equal to each other ($\sigma_x = \sigma_y = P_c$). For $x \rightarrow a/2$ (i.e., as one approaches the crown of the slit) σ_y is equal to about $0.68 P_c$ for $b = 3 \text{ mm}$ while for $b = 0.6 \text{ mm}$ σ_y becomes equal to $4.3 P_c$. In other words, for the narrower slit the transverse normal stress is more than 6 times higher from the respective stress in the wider slit. For the longitudinal normal stress σ_x things are equally emphatic: its maximum value recorded in the immediate vicinity of the slit’s crown is less than $0.1 P_c$ for the wide slit while it even exceeds $0.6 P_c$ for the narrow one.

For the second loading type (i.e., tension at $\phi_o = 90^\circ$), the stress components along the longitudinal symmetry axis of the slit are plotted (normalized again over P_c and using either Eqs. 31 or 33) in Fig. 7a, b. As it can be seen from these figures the variation of the normal stresses σ_x and σ_y (the shear ones are obviously zero) is completely different compared to the previous case (i.e., for compression at $\phi_o = 0^\circ$) for both the wide and the narrow slits. Indeed, both stresses are now tensile all along the specific locus. Moreover, from a quantitative point of view, the transverse normal stress σ_y attains considerably higher values as one approaches the slit’s crown. It is mentioned characteristically that for $b = 0.6 \text{ mm}$ the magnitude of σ_y is equal to $8.7 P_c$, a value which is more than two times

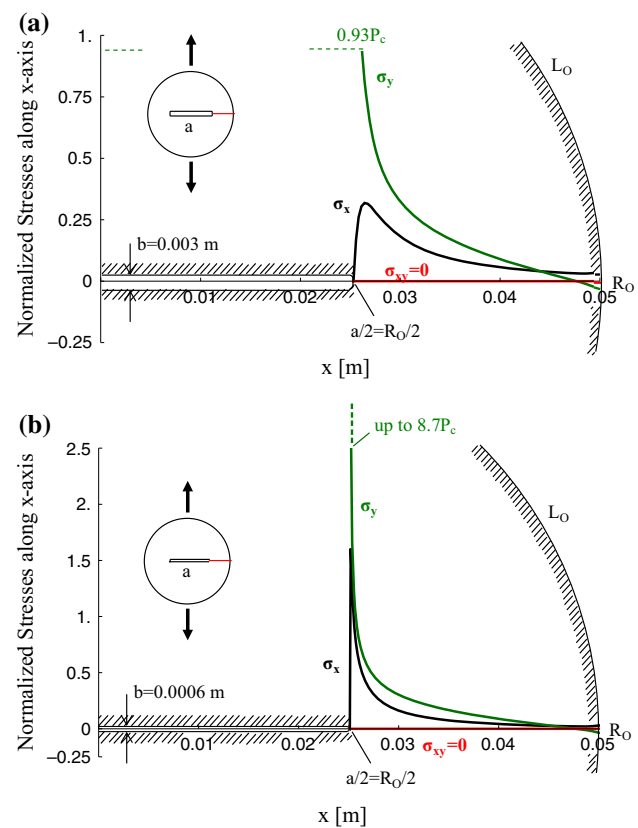


Fig. 7 The stress field along the slit’s longitudinal axis of symmetry for $b = 3 \text{ mm}$ (a) and $b = 0.6 \text{ mm}$ (b) for tension normal ($\phi_o = 90^\circ$) to the slit’s longitudinal axis

higher compared to the respective one recorded for the configuration for compression at $\phi_o = 0^\circ$. Similar conclusions are drawn for the longitudinal normal stress σ_x which for the narrow slit ($b = 0.6 \text{ mm}$) and as $x \rightarrow a/2$ attains values exceeding $1.5 P_c$, again two times higher from the respective value attained for the configuration for compression at $\phi_o = 0^\circ$.

4.2 The Stress Field along the Perimeter of the Slit for Compression at $\phi_o = 0^\circ$ and for Tension at $\phi_o = 90^\circ$ (Mode-I Loading Conditions)

The second locus of increased importance is the perimeter of the slit itself. For practical reasons the exploration of the stress field along this locus is implemented in terms of curvilinear (Eq. 33) rather than Cartesian coordinates, as it is clearly outlined in Fig. 5. Again two characteristic configurations are considered corresponding to a very narrow slit (approaching a ‘mathematical’ crack with a single tip at each end, or in other words with the corner point A_1 almost coinciding with the middle point $M(a/2, 0)$ of the slit’s short edge (see the sketch embedded in Fig. 8)

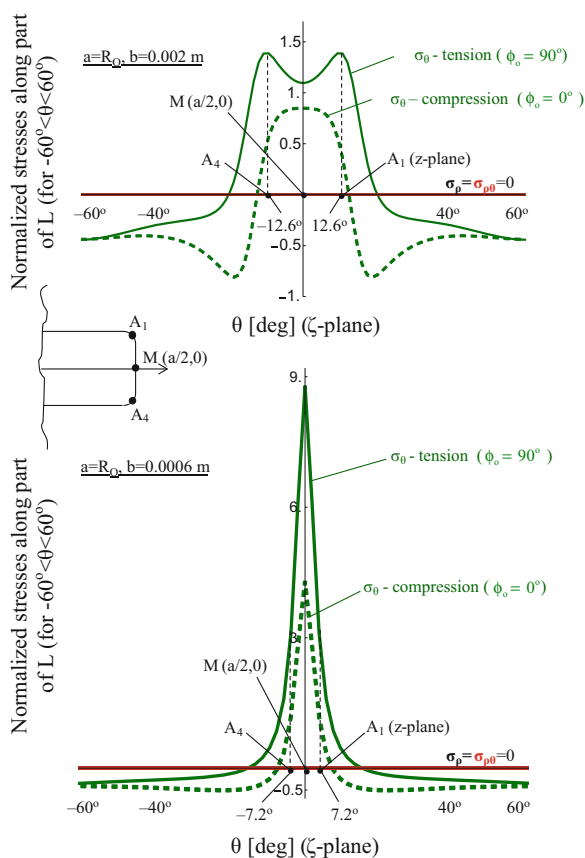


Fig. 8 The variation of the normal transverse stress σ_θ along the slit's perimeter around the vicinity of the slit's crown, for compression at $\phi_o = 0^\circ$ and tension at $\phi_o = 90^\circ$ for $b = 2$ mm (a) and $b = 0.6$ mm (b)

and to a wider one (i.e., with two distinct corner points A_4 , A_1 and A_2 , A_3 at each one of its ends).

The geometric features of the configuration considered are similar to the respective ones of Sect. 4.1, apart from the width b of the wider slit which is now considered equal to 2 mm (a value which is very close to the average width of most slits machined mechanically in practice by means of rotating cutting discs). The respective distributions of the single non-zero stress component normalized against P_c , i.e., the transverse normal stress σ_θ (for obvious reasons it holds that along the locus here considered $\sigma_\rho = \sigma_{\rho\theta} = 0$) are plotted in Fig. 8a, b. The differences between the two configurations are striking for both loading modes, i.e., for compression at $\phi_o = 0^\circ$ and tension at $\phi_o = 90^\circ$. Besides the quantitative deviations concerning the magnitude of the stress (which are more or less expected), impressive qualitative differences appear concerning the points at which the stress is maximized. Indeed, as it can be seen from Fig. 8a, which corresponds to the wider slit with $b = 2$ mm, in case of compression along the slit's longitudinal symmetry axis (i.e., $\phi_o = 0^\circ$), the magnitude of the

stress is maximized at point $M(a/2, 0)$ (see the dotted line in Fig. 8a). The normalized value of σ_θ at point $M(a/2, 0)$ is equal to about $0.85 P_c$. From this point the stress magnitude decreases smoothly. At the corner of the slit in the first quadrant (point A_1), which for the specific geometry corresponds to an angle $\theta = 12.6^\circ$ in the ζ -plane, σ_θ attains a value equal to about $0.45 P_c$, which is almost 50 % lower from the maximum value attained at point $M(a/2, 0)$. As one moves away from point A_1 towards the slit's short axis of symmetry, the stress keeps decreasing and at about $\theta = 15^\circ$ it changes sign becoming compressive. A clear minimum at about $\theta = 20^\circ$, of magnitude about equal to the maximum one attained at $\theta = 0^\circ$, characterizes the distribution.

In case a tensile load (equal in absolute value to the previous compressive one) is applied normally to the slit's longitudinal axis of symmetry ($\phi_o = 90^\circ$), things are completely different. The stress is maximized at the corner point A_1 rather than at the mid-point $M(a/2, 0)$. Indeed, at A_1 the value of σ_θ is equal to about $1.45 P_c$ while at point $M(a/2, 0)$ the respective value is equal to about $1.10 P_c$ or comparatively 30 % lower.

Consider now the narrow slit ($b = 0.6$ mm), for which the distribution of σ_θ along the slit's perimeter is plotted in Fig. 8b: for both loading modes (i.e., compression at $\phi_o = 0^\circ$ and tension at $\phi_o = 90^\circ$), the stress is maximized at $\theta = 0^\circ$, i.e., at point $M(a/2, 0)$. The magnitude of σ_θ at $M(a/2, 0)$ is equal to $8.7 P_c$ and $4.3 P_c$, for tension at $\phi_o = 90^\circ$ and compression at $\phi_o = 0^\circ$, respectively. The values corresponding to point A_1 (for the specific geometry it is located at $\theta = 7.2^\circ$) are considerably lower. Indeed, at point A_1 σ_θ is equal to about $1.0 P_c$ and $2.0 P_c$, respectively, i.e., less than one-fourth of the respective ones at point $M(a/2, 0)$.

The above-outlined features of the stress distribution around the slit's perimeter indicate clearly that the amplification of the stress field in the immediate vicinity of the slit's crown strongly depends on the relative dimensions of the slit, i.e., on the a/b ratio. In this context, an attempt is described in Sect. 5 to quantify this dependence, since it is of crucial practical importance, given that it governs the values of the fracture toughness obtained in case discs with mechanically machined slits rather than with 'mathematical' cracks are tested.

5 The Stress Concentration Around the Crown of Rectangular Slits

The amplification of a stress field in the presence of a geometrical discontinuity is characterized by either the Stress Intensity Factor—SIF (assuming that the discontinuity is a 'mathematical' crack, which in turn results to

infinite values of the stress component at the crack's tip) or by the Stress Concentration Factor—SCF (assuming the stress field components remain bounded all over the body including the immediate vicinity of the discontinuity itself). It is evident that in case the distance between the discontinuity's lips is non-zero the concept of the SIF becomes inapplicable. Therefore, for the configurations considered in this work one should resort to the SCF concept to characterize the amplification of the stress field in the immediate vicinity of the slit's crown.

In this context, the Stress Concentration Factor, defined here as the ratio of σ_θ over the amplitude P_c of the parabolic distribution of the externally applied load, is plotted in Fig. 9a, b against the width b of the slit, assuming that the respective slit's length is kept constant, equal to $a = R_0$. The remaining geometric characteristics of the disc's configuration are the same as in Sect. 4. The values

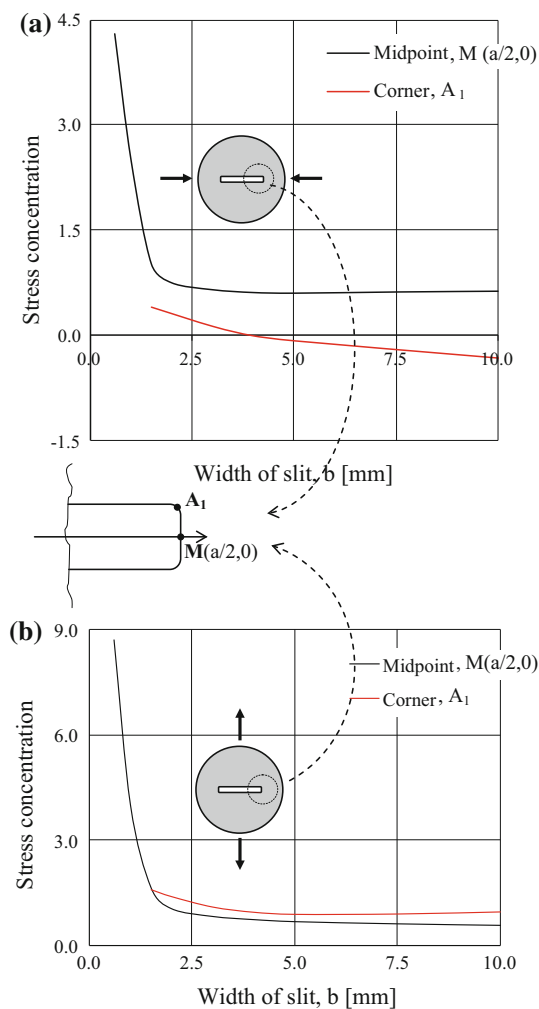


Fig. 9 The stress concentration at the slit's mid-point $M(a/2, 0)$ and at the slit's corner A_1 for: **a** compression at $\phi_o = 0^\circ$ and **b** tension at $\phi_o = 90^\circ$

considered for the parameter b are within the $0.5 \text{ mm} < b < 10 \text{ mm}$ range, which covers most slits machined in praxis for the determination of fracture toughness.

Taking into account the conclusions drawn in Sect. 4, two points of the slit's perimeter are considered, namely the mid-point $M(a/2, 0)$ and the corner point A_1 . In case of compressive load applied at $\phi_o = 0^\circ$, i.e., along the slit's longitudinal axis of symmetry, the results are plotted in Fig. 9a. It is seen from this figure that independently of b the stress field is more intense at the mid-point $M(a/2, 0)$, rather than at the corners of the slit. Moreover, for $b > 2 \text{ mm}$ the stress concentration appears to be insensitive to any variation of the distance between the slit's lips (at least for the specific disc's geometrical features). Only for $b < 2 \text{ mm}$ the stress concentration starts increasing abruptly attaining values equal to about 4.5 for $b = 0.5 \text{ mm}$, remaining in any case bounded. Concerning the stress concentration at point A_1 , it increases more or less smoothly for decreasing b , remaining lower than that at point $M(a/2, 0)$ for the whole range of b values considered. What is to be noticed is that for $b > 4 \text{ mm}$ the stress concentration factor at A_1 is negative which means that the stress field at A_1 is of compressive nature preventing, perhaps, rather than favoring crack initiation.

In case of tensile load applied at $\phi_o = 90^\circ$, i.e., normally to the slit's longitudinal axis of symmetry, the respective variation of the stress concentration is plotted in Fig. 9b. Again, for b values exceeding 2 mm, the role of the distance between the slit's lips is not significant, both for the mid-point $M(a/2, 0)$ and the corner point A_1 . What is different, however, for the specific loading mode is that for $b > 2 \text{ mm}$ the stress concentration at the corner point A_1 exceeds the respective one at point $M(a/2, 0)$, indicating that crack initiation could be expected from the corner of the slit rather than from its mid-point, somehow violating symmetry arguments. From a quantitative point of view, the stress field amplification is much more pronounced for tension at $\phi_o = 90^\circ$, especially for b values lower than 2 mm. It is mentioned characteristically that the stress concentration factor attains a value equal to about 9 for $b = 0.5 \text{ mm}$. Moreover, for the whole range of b values the stress concentration factor is positive for both points $M(a/2, 0)$ and A_1 .

Before concluding this section one should consider, even shortly, what happens for configurations with inclination of the slit's long axis of symmetry other than $\phi_o = 90^\circ$ and $\phi_o = 0^\circ$, i.e., configurations for which the double symmetry of geometry and loading is lost. The main problem now is that due to the non-symmetric shape of the deformed slit the four corners are not any more equivalent to each other. For a quantitative exploration of this aspect, i.e., the determination of stress concentration for

asymmetric configurations, combined knowledge of the deformation and stress fields in the immediate vicinity of the tips is required. Taking advantage of results from an ongoing research project (Markides and Kourkoulis 2015b), the deformed disc's shape for a characteristic geometry with $\phi_o = 45^\circ$ is shown in Fig. 10a together with the respective stress tensors for tips A_1 and A_4 . It is clearly seen that the two tips are not equivalent neither concerning the stress field nor the deformation mode: tip A_1 is under opening mode while tip A_4 is under closing mode. Therefore, a unique SCF cannot be defined for the specific problem.

Assuming that fracture will probably start from the tip under opening mode (tip A_1 in this case) rather than from the tip under closing mode or the mid-point of the short edge b , it would be interesting to consider the stress amplification at tip A_1 . Even for a single tip, however, the problem of defining the SCF remains since the lack of symmetry does not permit a priori knowledge of the crack initiation and propagation path. One possible solution could be to consider the ratio of the equivalent stress at the

specific tip normalized over the parameter P_c . The variation of this quantity against ϕ_o is plotted in next Fig. 10b, the main characteristic of which is the lack of any symmetric feature. In any case, the specific point should be considered in more details and in combination with a proper fracture criterion which will definitely indicate the fracture initiation point.

6 Transitioning from Stress Concentration to Stress Intensity

Despite its inadequacy to describe the local stress field around the tips of a slit of finite b/a ratio, the importance of SIFs remains crucial from a theoretical point of view since it designates the limiting case for which b/a tends to zero. It is, therefore, worth providing closed-form expressions for the SIFs assuming that the slit approaches a 'mathematical' crack. In this direction, the formulae of Eqs. (4) and (5), providing $\omega(\zeta)$, will first be written in a most appropriate, for this case, form. Namely, setting $z = a/2$ in Eq. (4), so that $\zeta = 1$, and solving for b , it is obtained:

$$b = a \left[1 + \sum_{\ell=1}^{\infty} (-1)^\ell c_\ell \right] \left(1 + \sum_{\ell=1}^{\infty} c_\ell \right)^{-1} \tag{34}$$

Introducing now Eq. (34) in Eq. (5) it follows that:

$$R = \frac{a}{2} \left(1 + \sum_{\ell=1}^{\infty} c_\ell \right)^{-1} \tag{35}$$

Substituting Eq. (35) in Eq. (4) an alternative expression for the conformal mapping is obtained in terms of parameter a rather than in terms of b [entering in Eq. (4) through Eq. (5)] as:

$$z = \frac{a}{2} \left(1 + \sum_{\ell=1}^{\infty} c_\ell \right)^{-1} \left(\zeta + \sum_{\ell=1}^{\infty} \frac{c_\ell}{\zeta^{2\ell-1}} \right) \tag{36}$$

Consider now that b tends to zero, i.e., that the slit L tends to the straight cut ('mathematical' crack) of length a . Obviously, k tends to zero and, therefore, $\beta = e^{i2k\pi}$, appearing in Eq. (6), becomes unity. Then, all coefficients c_ℓ in Eq. (6) vanish, except c_1 which becomes unity. In this context, Eq. (36) reduces to the simpler one:

$$z = \frac{a}{4} \left(\zeta + \frac{1}{\zeta} \right) \tag{37}$$

It is now evident that Eq. (37) represents, also, the limiting case $b/2 \rightarrow 0$ in the well-known transformation:

$$z = R' \left(\zeta + \frac{m}{\zeta} \right); \quad R' = \frac{a/2 + b/2}{2}; \quad m = \frac{a/2 - b/2}{a/2 + b/2} \tag{38}$$

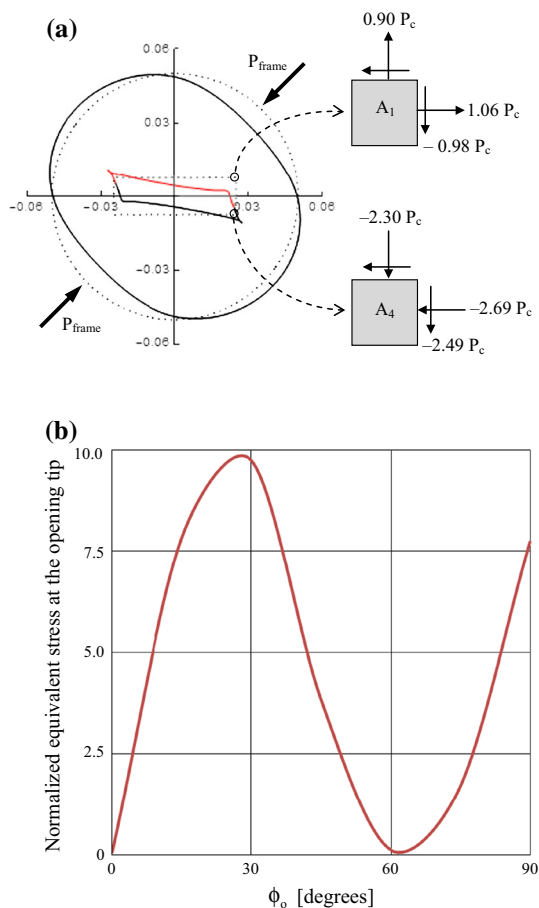


Fig. 10 a Initial and deformed configuration of a disc with a rectangular slit and the stress components at the two corners. b The normalized equivalent stress at the tip under opening mode (tip A_1)

which conformally maps the outside of an elliptical hole of major and minor semi-axes $a/2$ and $b/2$, respectively, on the outside of the unit circle γ . In other words, Eq. (37) describes also the case when an elliptical hole of total length a tends to a ‘mathematical’ crack.

The above observation is of utmost importance since it points out that in the limiting case when $b \rightarrow 0$ the solution introduced in the present paper for the disc with a rectangular slit of length a completely coincides with that of the disc with an elliptical hole of major semi-axis $a/2$ (Markides and Kourkoulis 2014a, b). Therefore, the expressions for the SIFs describing the stress field around the crown of a rectangular slit the width of which tends to zero are identical to those obtained by Markides and Kourkoulis (2014b), for the case of a circular disc with an elliptical hole when its minor semi-axis tends to zero. For the nomenclature adopted in the present case, these expressions read as:

$$K_I = P_c \sqrt{\frac{a}{2\pi}} \left\{ 2b_0 + \Re B'_0 + \frac{a^2}{2} \left(\Re B_2 + \frac{\Re B'_2}{4} \right) + \sum_{n=1}^{\infty} \left(\frac{a}{4} \right)^{4n} \left[\Re B_{4n} \left(\frac{G_{4n+1}^{\infty}}{4n+1} - G_{4n}^0 \right) - \frac{\Re B'_{4n}}{4n+1} G_{4n+1}^0 + \frac{a^2}{16} \left(\Re B_{2(2n+1)} \left(\frac{G_{4n+3}^{\infty}}{4n+3} - G_{2(2n+1)}^0 \right) - \frac{\Re B'_{2(2n+1)}}{4n+3} G_{4n+3}^0 \right) \right] \right\} \quad (39)$$

$$K_{II} = P_c \sqrt{\frac{a}{2\pi}} \left\{ \Im B'_0 + \frac{a^2}{4} \left(\Im B_2 + \frac{\Im B'_2}{2} \right) - \sum_{n=1}^{\infty} \left(\frac{a}{4} \right)^{4n} \left[\Im B_{4n} \left(\frac{G_{4n+1}^{\infty}}{4n+1} + G_{4n}^0 \right) + \frac{\Im B'_{4n}}{4n+1} G_{4n+1}^0 + \frac{a^2}{16} \left(\Im B_{2(2n+1)} \left(\frac{G_{4n+3}^{\infty}}{4n+3} + G_{2(2n+1)}^0 \right) + \frac{\Im B'_{2(2n+1)}}{4n+3} G_{4n+3}^0 \right) \right] \right\} \quad (40)$$

7 Discussion and Conclusions

An analytic solution for the stress field in a circular finite disc with a central rectangular slit with rounded corners was developed. The solution provides the stress components at any point on the disc’s surface. The stress field along two characteristic loci of increased practical importance was discussed in detail. Moreover, two loading types were studied, i.e., compression along the slit’s longitudinal axis of symmetry and tension normal to this axis.

The principal innovative point of the solution described is that it takes into account the exact geometry of the discontinuity without resorting to simplifying assumptions as it is for example the concept of a ‘mathematical’ crack, or of a relatively short crack with respect to the disc’s radius. Moreover, the load distribution considered, i.e., a parabolic distribution of radial stresses along two finite arcs of the disc’s periphery, approaches very closely the actual

distribution in case a disc is squeezed between metallic jaws of given finite curvature.

Before recapitulating the conclusions drawn in previous sections, a few words about the scheme adopted for validating the solution introduced are necessary. While the touchstone for an analytic solution is to compare its results with experimental evidence, it is to be accepted that the respective tests are very difficult to be implemented. It was, therefore, decided to assess the present solution against a properly validated numerical model (Kourkoulis et al. 2015b). In this context, a finite element model was prepared for both the disc and the jaw, considering that the test is realized according to the ISRM suggestions for the intact Brazilian-disc test. Both the disc and the jaw were simulated using 2D plane stress (with thickness) finite elements. The geometry and material properties of the disc and the jaws matched exactly those considered in the theoretical analysis. The disc was

assumed to be in frictionless contact with the jaws, since the same assumption was adopted in the analytic solution. The Finite Element model was meshed using about 7000 4-node elements (Plane182). The density of the mesh was calibrated to eliminate any mesh dependency phenomena. The simulations were performed using the commercially available software ANSYS12.

Prior to using the numerical model for the needs of the present study, its outcomes were compared (for validation reasons) with the analytic results obtained by Markides et al. (2011) for the stress field in a circular disc with a short central ‘mathematical’ crack (in fact a very small value was assigned to b , $b = 0.1$ mm) under uniform radial pressure along a predefined arc of the disc’s periphery. The comparison was satisfactory for the whole range of crack inclination angles for which no contact forces appear ($0^\circ \leq \phi_o \leq 29.3^\circ$) and, therefore, the model can be considered reliable.

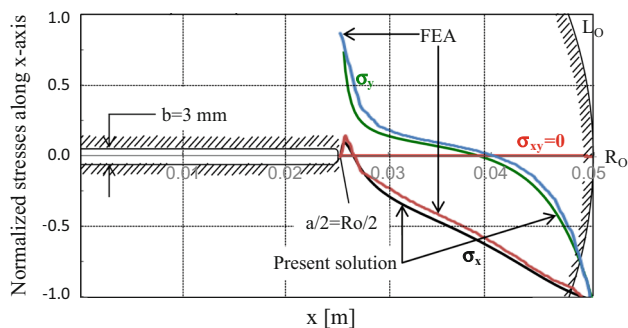


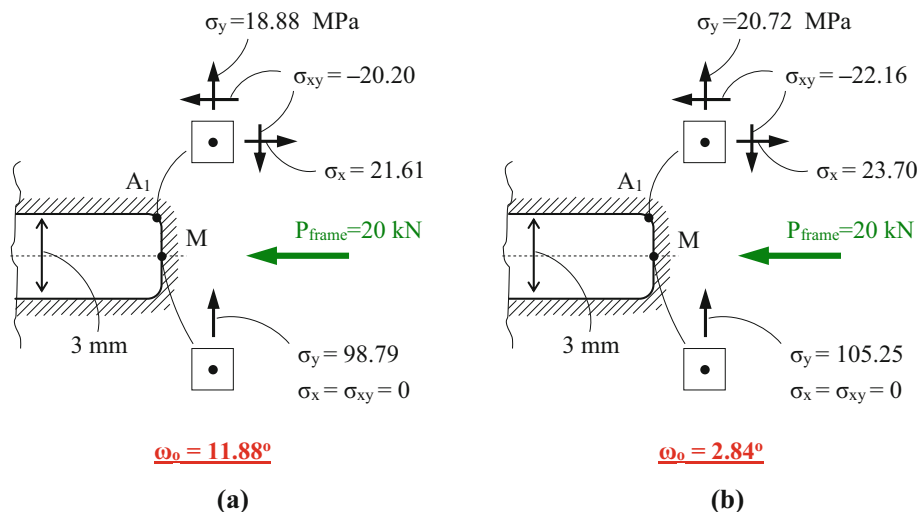
Fig. 11 Numerical versus analytic results for the stress field along the longitudinal slit's axis of symmetry

As a next step, the above-validated numerical model was used for the calculation of the stress field components in a circular disc with a central rectangular slit ($a = R_o = 50 \text{ mm}$ and $b = 3 \text{ mm}$) oriented along the vertical axis of symmetry of the configuration (i.e., $\phi_o = 0^\circ$). The results for the stresses developed along the locus with $\phi = 0^\circ$ (i.e., along the longitudinal symmetry axis of the slit) are plotted (normalized against the amplitude of the pressure induced by the jaw on the disc) in Fig. 11 in juxtaposition to the respective results of the analytic solution. The agreement can be considered quite satisfactory. Some discrepancies, not exceeding 5 %, can be well attributed to the fact that the length of the loaded arc adopted in the analytic solution is obtained from the solution of the intact disc-jaw contact problem and it is somehow smaller from the arc developed during the compression of the disc weakened by a rectangular slit. Although this difference is relatively small [in accordance with a previous study for the contact arc in case circular rings with small inner radius are compressed between the ISRM jaws (Kourkoulis et al. 2015a)], it should not be ignored (especially for a values exceeding half of the disc's radius length, as it is the case considered here).

The main conclusion drawn from the present study is related to the role of the slit's width b on the stress field in the immediate vicinity of the slit's crown and also to the quantification of the variation of the stress concentration factor from the slit's corner A_1 to the slit's mid-point $M(a/2, 0)$. It was revealed that the maximum stress concentration (and, therefore, the potential crack initiation point) 'travels' from A_1 to $M(a/2, 0)$ and vice versa depending on the exact combination of b and ϕ_o . In other words, depending on the distance between the slit's lips, the superposition of the 'action' of the concentration due to the two adjacent corner points A_4 and A_1 can result in either amplification or weakening of the stress field on the mid-point $M(a/2, 0)$ of the slit. It should be emphasized at this point that the above conclusions are drawn for a disc with specific geometric characteristics and also with a relatively "long" contact rim. Things could change (at least quantitatively) in case of discs made of stiffer materials. This is clearly depicted in Fig. 12 where the components of the stress tensor are shown as they are calculated for two discs made of materials with significantly different stiffness: Fig. 12a corresponds to a disc made of PMMA which results to a half contact rim $\omega_o = 11.88^\circ$ while Fig. 12b corresponds to a disc made of Dionysos marble which results to half contact rim $\omega_o = 2.84^\circ$.

Besides the role of b and its paramount influence on the stress field amplification, it was also revealed that the two loading types studied (i.e., compression at $\phi_o = 0^\circ$ and tension at $\phi_o = 90^\circ$) are not equivalent although this is the underlying principle for adopting the validity of results concerning the Mode-I fracture toughness as they are obtained from tests with either CSTBD and CCNBD specimens. To further enlighten the specific point, the variation of the equivalent stress along the slit's longitudinal symmetry axis ($a/2 < x < R_o$, $y = 0$, with $a = R_o$), normalized against P_c , is plotted in Fig. 13a for both loading types and for a relatively wide slit with $b = 3 \text{ mm}$.

Fig. 12 The stress tensor at the slit's crown for two discs made of materials with different stiffness. Disc made of: **a** PMMA and **b** Dionysos marble



It is seen from this figure that all along the specific locus the two distributions are critically different from each other. Moreover, the compressive loading type results in considerably lower equivalent stress as one approaches the notch crown. It could be, therefore, suggested (despite the fact that the present analysis is purely linear elastic and, therefore, no conclusions about fracture and crack initiation should be drawn) that the values of K_{IC} determined by compressing a disc parallel to the slit will overestimate the actual fracture toughness of the material (considering that K_{IC} characterizes the resistance of a material to the initiation and propagation of a crack under Mode-I loading conditions, i.e., under tensile loads).

The above conclusions can be further supported by plotting the stress concentration factor at the mid-point $M(a/2, 0)$ for compression at $\phi_o = 0^\circ$ and tension at $\phi_o = 90^\circ$, against the slit width b . These plots, shown in

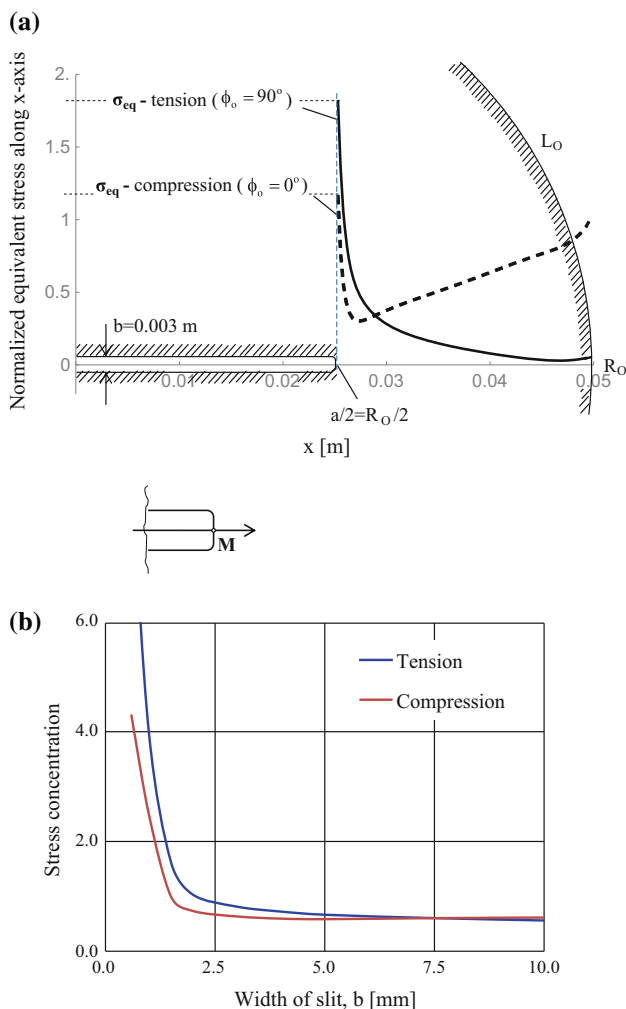


Fig. 13 **a** Variation of the equivalent stress along the slit's longitudinal symmetry axis and **b** the stress concentration for compression at $\phi_o = 0^\circ$ and tension at $\phi_o = 90^\circ$ against the slit's width b

Fig. 13b, reveal again that only for slit's widths exceeding 5 mm the two loading types are more or less equivalent. However, slits with $b > 5$ mm can be hardly considered as representing in a satisfactory manner actual cracks. On the contrary, for $b < 5$ mm the stress concentration factor for tensile loading mode increases more abruptly compared to the respective increase for compressive loading mode.

Finally, it is emphasized again that the present study should be only considered as a first step in the direction of assessing the standardized tests used for the experimental determination of K_{IC} . There are two reasons for this: firstly, there are some critical assumptions adopted. For example, the material is assumed to be linear elastic and no fracture criteria were incorporated in the analysis. Moreover, only a finite number of terms of the infinite series were taken into account for manageable formulae to be obtained for the complex potentials and the stress components. Secondly, there are quite a few additional parameters that should be taken into account and quantified, before a definite assessment of the transition from the CSTBD configuration to that of the CCNBD, so that one could take into account the actual role of the finite distance between the lips of the discontinuity.

The above discussion by no means deteriorates the value of the analysis described in the present paper. The closed-form formulae introduced for the complex potentials and the stress field could be proven valuable, for example, in the direction of validating sophisticated numerical models permitting thorough parametric analyses. Clearly, the crucial step in the direction of definitely assessing the results of the above-mentioned standardized tests necessitates huge effort and combined analytic, experimental and numerical investigations, well beyond the isolated attempts of independent researchers. This decisive step could be only implemented as team work of working groups or technical committees under the auspices of prestigious international scientific societies as it is for example ISRM and ASTM.

Acknowledgments The research described in this paper is co-financed by the EU (European Social Fund-ESF) and Greek national funds through the Operational Program "Education and Lifelong Learning" of the National Strategic Reference Framework (NSRF)—Research Funding Program: THALES: Reinforcement of the interdisciplinary and/or inter-institutional research and innovation. The authors are indebted to Dr. Panagiotis Chatzistergos of the Staffordshire University, Stoke-on-Trent, UK, for his valuable contribution during the numerical modeling. Finally, the authors would like to thank the anonymous reviewers of the initial version of the manuscript for their most valuable suggestions.

Appendix

Principal parts of the following functions in brackets, appearing in Eqs. (28), (29), (39) and (40)

$$\begin{aligned}
 G_{4n+1}^{(\infty)}(\zeta) &:= P.P. \left[\left(\zeta + \frac{c_1}{\zeta} + \frac{c_2}{\zeta^3} + \frac{c_3}{\zeta^5} + \frac{c_4}{\zeta^7} + \frac{c_5}{\zeta^9} + \frac{c_6}{\zeta^{11}} \right)^{4n+1} \right] \\
 &= \sum_{k_1=0}^{4n+1} \cdot \sum_{k_2=0}^{4n+1-k_1} \cdot \sum_{k_3=0}^{4n+1-(k_1+k_2)} \cdot \sum_{k_4=0}^{4n+1-(k_1+k_2+k_3)} \cdot \sum_{k_5=0}^{4n+1-(k_1+k_2+k_3+k_4)} \cdot \sum_{k_6=0}^{\frac{4n+1}{2} - (6k_1+5k_2+4k_3+3k_4+2k_5)} \\
 &\quad \frac{(4n+1)! c_6^{k_1} c_5^{k_2} c_4^{k_3} c_3^{k_4} c_2^{k_5} c_1^{k_6}}{k_1! k_2! k_3! k_4! k_5! k_6! (4n+1-k_1-k_2-k_3-k_4-k_5-k_6)!} \zeta^{4n+1-2(6k_1+5k_2+4k_3+3k_4+2k_5+k_6)} \\
 G_{4n}^{(0)}(\zeta) &:= P.P. \left[\left(\zeta + \frac{c_1}{\zeta} + \frac{c_2}{\zeta^3} + \frac{c_3}{\zeta^5} + \frac{c_4}{\zeta^7} + \frac{c_5}{\zeta^9} + \frac{c_6}{\zeta^{11}} \right) \left(\frac{1}{\zeta} + c_1 \zeta + c_2 \zeta^3 + c_3 \zeta^5 + c_4 \zeta^7 + c_5 \zeta^9 + c_6 \zeta^{11} \right)^{4n} \right] = \\
 &\quad \sum_{k_1=0}^{4n} \cdot \sum_{k_2=0}^{4n-k_1} \cdot \sum_{k_3=0}^{4n-(k_1+k_2)} \cdot \sum_{k_4=0}^{4n-(k_1+k_2+k_3)} \cdot \sum_{k_5=0}^{4n-(k_1+k_2+k_3+k_4)} \cdot \sum_{k_6=0}^{2n-1-(6k_1+5k_2+4k_3+3k_4+2k_5)} \\
 &\quad \frac{(4n)! c_6^{k_1} c_5^{k_2} c_4^{k_3} c_3^{k_4} c_2^{k_5} c_1^{k_6}}{k_1! k_2! k_3! k_4! k_5! k_6! (4n-k_1-k_2-k_3-k_4-k_5-k_6)!} \zeta^{-4n+1+2(6k_1+5k_2+4k_3+3k_4+2k_5+k_6)} + \\
 &\quad \sum_{k_1=0}^{4n} \cdot \sum_{k_2=0}^{4n-k_1} \cdot \sum_{k_3=0}^{4n-(k_1+k_2)} \cdot \sum_{k_4=0}^{4n-(k_1+k_2+k_3)} \cdot \sum_{k_5=0}^{4n-(k_1+k_2+k_3+k_4)} \cdot \sum_{k_6=0}^{2n-(6k_1+5k_2+4k_3+3k_4+2k_5)} \\
 &\quad \frac{(4n)! c_6^{k_1} c_5^{k_2} c_4^{k_3} c_3^{k_4} c_2^{k_5} c_1^{k_6+1}}{k_1! k_2! k_3! k_4! k_5! k_6! (4n-k_1-k_2-k_3-k_4-k_5-k_6)!} \zeta^{-(4n+1)+2(6k_1+5k_2+4k_3+3k_4+2k_5+k_6)} + \\
 &\quad \sum_{k_1=0}^{4n} \cdot \sum_{k_2=0}^{4n-k_1} \cdot \sum_{k_3=0}^{4n-(k_1+k_2)} \cdot \sum_{k_4=0}^{4n-(k_1+k_2+k_3)} \cdot \sum_{k_5=0}^{4n-(k_1+k_2+k_3+k_4)} \cdot \sum_{k_6=0}^{2n+1-(6k_1+5k_2+4k_3+3k_4+2k_5)} \\
 &\quad \frac{(4n)! c_6^{k_1} c_5^{k_2} c_4^{k_3} c_3^{k_4} c_2^{k_5+1} c_1^{k_6}}{k_1! k_2! k_3! k_4! k_5! k_6! (4n-k_1-k_2-k_3-k_4-k_5-k_6)!} \zeta^{-(4n+3)+2(6k_1+5k_2+4k_3+3k_4+2k_5+k_6)} + \\
 &\quad \sum_{k_1=0}^{4n} \cdot \sum_{k_2=0}^{4n-k_1} \cdot \sum_{k_3=0}^{4n-(k_1+k_2)} \cdot \sum_{k_4=0}^{4n-(k_1+k_2+k_3)} \cdot \sum_{k_5=0}^{4n-(k_1+k_2+k_3+k_4)} \cdot \sum_{k_6=0}^{2(n+1)-(6k_1+5k_2+4k_3+3k_4+2k_5)} \\
 &\quad \frac{(4n)! c_6^{k_1} c_5^{k_2+1} c_4^{k_3} c_3^{k_4+1} c_2^{k_5} c_1^{k_6}}{k_1! k_2! k_3! k_4! k_5! k_6! (4n-k_1-k_2-k_3-k_4-k_5-k_6)!} \zeta^{-(4n+5)+2(6k_1+5k_2+4k_3+3k_4+2k_5+k_6)} + \\
 &\quad \sum_{k_1=0}^{4n} \cdot \sum_{k_2=0}^{4n-k_1} \cdot \sum_{k_3=0}^{4n-(k_1+k_2)} \cdot \sum_{k_4=0}^{4n-(k_1+k_2+k_3)} \cdot \sum_{k_5=0}^{4n-(k_1+k_2+k_3+k_4)} \cdot \sum_{k_6=0}^{2n+3-(6k_1+5k_2+4k_3+3k_4+2k_5)} \\
 &\quad \frac{(4n)! c_6^{k_1} c_5^{k_2} c_4^{k_3+1} c_3^{k_4} c_2^{k_5} c_1^{k_6}}{k_1! k_2! k_3! k_4! k_5! k_6! (4n-k_1-k_2-k_3-k_4-k_5-k_6)!} \zeta^{-(4n+7)+2(6k_1+5k_2+4k_3+3k_4+2k_5+k_6)} + \\
 &\quad + \sum_{k_1=0}^{4n} \cdot \sum_{k_2=0}^{4n-k_1} \cdot \sum_{k_3=0}^{4n-(k_1+k_2)} \cdot \sum_{k_4=0}^{4n-(k_1+k_2+k_3)} \cdot \sum_{k_5=0}^{4n-(k_1+k_2+k_3+k_4)} \cdot \sum_{k_6=0}^{2(n+2)-(6k_1+5k_2+4k_3+3k_4+2k_5)} \\
 &\quad \frac{(4n)! c_6^{k_1} c_5^{k_2+1} c_4^{k_3} c_3^{k_4} c_2^{k_5} c_1^{k_6}}{k_1! k_2! k_3! k_4! k_5! k_6! (4n-k_1-k_2-k_3-k_4-k_5-k_6)!} \zeta^{-(4n+9)+2(6k_1+5k_2+4k_3+3k_4+2k_5+k_6)} + \\
 &\quad \sum_{k_1=0}^{4n} \cdot \sum_{k_2=0}^{4n-k_1} \cdot \sum_{k_3=0}^{4n-(k_1+k_2)} \cdot \sum_{k_4=0}^{4n-(k_1+k_2+k_3)} \cdot \sum_{k_5=0}^{4n-(k_1+k_2+k_3+k_4)} \cdot \sum_{k_6=0}^{2n+5-(6k_1+5k_2+4k_3+3k_4+2k_5)} \\
 &\quad \frac{(4n)! c_6^{k_1+1} c_5^{k_2} c_4^{k_3} c_3^{k_4} c_2^{k_5} c_1^{k_6}}{k_1! k_2! k_3! k_4! k_5! k_6! (4n-k_1-k_2-k_3-k_4-k_5-k_6)!} \zeta^{-(4n+11)+2(6k_1+5k_2+4k_3+3k_4+2k_5+k_6)}
 \end{aligned}$$

$$G_{4n+1}^{(0)}(\zeta) := P.P. \left[\left(\frac{1}{\zeta} + c_1 \zeta + c_2 \zeta^3 + c_3 \zeta^5 + c_4 \zeta^7 + c_5 \zeta^9 + c_6 \zeta^{11} \right)^{4n+1} \right]$$

$$= \sum_{k_1=0}^{4n+1} \cdot \sum_{k_2=0}^{4n+1-k_1} \cdot \sum_{k_3=0}^{4n+1-(k_1+k_2)} \cdot \sum_{k_4=0}^{4n+1-(k_1+k_2+k_3)} \cdot \sum_{k_5=0}^{4n+1-(k_1+k_2+k_3+k_4)} \cdot \sum_{k_6=0}^{2n-(6k_1+5k_2+4k_3+3k_4+2k_5)}$$

$$\frac{(4n+1)! c_6^{k_1} c_5^{k_2} c_4^{k_3} c_3^{k_4} c_2^{k_5} c_1^{k_6}}{k_1! k_2! k_3! k_4! k_5! k_6! (4n+1-k_1-k_2-k_3-k_4-k_5-k_6)!} \zeta^{-(4n+1)+2(6k_1+5k_2+4k_3+3k_4+2k_5+2k_6)}$$

$$G_{4n+3}^{(\infty)}(\zeta) := P.P. \left[\left(\zeta + \frac{c_1}{\zeta} + \frac{c_2}{\zeta^3} + \frac{c_3}{\zeta^5} + \frac{c_4}{\zeta^7} + \frac{c_5}{\zeta^9} + \frac{c_6}{\zeta^{11}} \right)^{4n+3} \right]$$

$$= \sum_{k_1=0}^{4n+3} \cdot \sum_{k_2=0}^{4n+3-k_1} \cdot \sum_{k_3=0}^{4n+3-(k_1+k_2)} \cdot \sum_{k_4=0}^{4n+3-(k_1+k_2+k_3)} \cdot \sum_{k_5=0}^{4n+3-(k_1+k_2+k_3+k_4)} \cdot \sum_{k_6=0}^{\frac{4n+3}{2} - (6k_1+5k_2+4k_3+3k_4+2k_5)}$$

$$\frac{(4n+3)! c_6^{k_1} c_5^{k_2} c_4^{k_3} c_3^{k_4} c_2^{k_5} c_1^{k_6}}{k_1! k_2! k_3! k_4! k_5! k_6! (4n+3-k_1-k_2-k_3-k_4-k_5-k_6)!} \zeta^{4n+3-2(6k_1+5k_2+4k_3+3k_4+2k_5+k_6)}$$

$$G_{2(2n+1)}^{(0)}(\zeta) := P.P. \left[\left(\zeta + \frac{c_1}{\zeta} + \frac{c_2}{\zeta^3} + \frac{c_3}{\zeta^5} + \frac{c_4}{\zeta^7} + \frac{c_5}{\zeta^9} + \frac{c_6}{\zeta^{11}} \right) \left(\frac{1}{\zeta} + c_1 \zeta + c_2 \zeta^3 + c_3 \zeta^5 + c_4 \zeta^7 + c_5 \zeta^9 + c_6 \zeta^{11} \right)^{2(2n+1)} \right] =$$

$$\sum_{k_1=0}^{2(2n+1)} \cdot \sum_{k_2=0}^{2(2n+1)-k_1} \cdot \sum_{k_3=0}^{2(2n+1)-(k_1+k_2)} \cdot \sum_{k_4=0}^{2(2n+1)-(k_1+k_2+k_3)} \cdot \sum_{k_5=0}^{2(2n+1)-(k_1+k_2+k_3+k_4)} \cdot \sum_{k_6=0}^{2n-(6k_1+5k_2+4k_3+3k_4+2k_5)}$$

$$\frac{[2(2n+1)]! c_6^{k_1} c_5^{k_2} c_4^{k_3} c_3^{k_4} c_2^{k_5} c_1^{k_6}}{k_1! k_2! k_3! k_4! k_5! k_6! [2(2n+1)-k_1-k_2-k_3-k_4-k_5-k_6]!} \zeta^{-(4n+1)+2(6k_1+5k_2+4k_3+3k_4+2k_5+k_6)} +$$

$$\sum_{k_1=0}^{2(2n+1)} \cdot \sum_{k_2=0}^{2(2n+1)-k_1} \cdot \sum_{k_3=0}^{2(2n+1)-(k_1+k_2)} \cdot \sum_{k_4=0}^{2(2n+1)-(k_1+k_2+k_3)} \cdot \sum_{k_5=0}^{2(2n+1)-(k_1+k_2+k_3+k_4)} \cdot \sum_{k_6=0}^{2n+1-(6k_1+5k_2+4k_3+3k_4+2k_5)}$$

$$\frac{[2(2n+1)]! c_6^{k_1} c_5^{k_2} c_4^{k_3} c_3^{k_4} c_2^{k_5} c_1^{k_6+1}}{k_1! k_2! k_3! k_4! k_5! k_6! [2(2n+1)-k_1-k_2-k_3-k_4-k_5-k_6]!} \zeta^{-(4n+3)+2(6k_1+5k_2+4k_3+3k_4+2k_5+k_6)}$$

$$+ \sum_{k_1=0}^{2(2n+1)} \cdot \sum_{k_2=0}^{2(2n+1)-k_1} \cdot \sum_{k_3=0}^{2(2n+1)-(k_1+k_2)} \cdot \sum_{k_4=0}^{2(2n+1)-(k_1+k_2+k_3)} \cdot \sum_{k_5=0}^{2(2n+1)-(k_1+k_2+k_3+k_4)} \cdot \sum_{k_6=0}^{2(n+1)-(6k_1+5k_2+4k_3+3k_4+2k_5)}$$

$$\frac{[2(2n+1)]! c_6^{k_1} c_5^{k_2} c_4^{k_3} c_3^{k_4} c_2^{k_5+1} c_1^{k_6}}{k_1! k_2! k_3! k_4! k_5! k_6! [2(2n+1)-k_1-k_2-k_3-k_4-k_5-k_6]!} \zeta^{-(4n+5)+2(6k_1+5k_2+4k_3+3k_4+2k_5+k_6)} +$$

$$\sum_{k_1=0}^{2(2n+1)} \cdot \sum_{k_2=0}^{2(2n+1)-k_1} \cdot \sum_{k_3=0}^{2(2n+1)-(k_1+k_2)} \cdot \sum_{k_4=0}^{2(2n+1)-(k_1+k_2+k_3)} \cdot \sum_{k_5=0}^{2(2n+1)-(k_1+k_2+k_3+k_4)} \cdot \sum_{k_6=0}^{2n+3-(6k_1+5k_2+4k_3+3k_4+2k_5)}$$

$$\frac{[2(2n+1)]! c_6^{k_1} c_5^{k_2} c_4^{k_3} c_3^{k_4+1} c_2^{k_5} c_1^{k_6}}{k_1! k_2! k_3! k_4! k_5! k_6! [2(2n+1)-k_1-k_2-k_3-k_4-k_5-k_6]!} \zeta^{-(4n+7)+2(6k_1+5k_2+4k_3+3k_4+2k_5+k_6)} +$$

$$\sum_{k_1=0}^{2(2n+1)} \cdot \sum_{k_2=0}^{2(2n+1)-k_1} \cdot \sum_{k_3=0}^{2(2n+1)-(k_1+k_2)} \cdot \sum_{k_4=0}^{2(2n+1)-(k_1+k_2+k_3)} \cdot \sum_{k_5=0}^{2(2n+1)-(k_1+k_2+k_3+k_4)} \cdot \sum_{k_6=0}^{2(n+2)-(6k_1+5k_2+4k_3+3k_4+2k_5)}$$

$$\frac{[2(2n+1)]! c_6^{k_1} c_5^{k_2} c_4^{k_3+1} c_3^{k_4} c_2^{k_5} c_1^{k_6}}{k_1! k_2! k_3! k_4! k_5! k_6! [2(2n+1)-k_1-k_2-k_3-k_4-k_5-k_6]!} \zeta^{-(4n+9)+2(6k_1+5k_2+4k_3+3k_4+2k_5+k_6)} +$$

$$\sum_{k_1=0}^{2(2n+1)} \cdot \sum_{k_2=0}^{2(2n+1)-k_1} \cdot \sum_{k_3=0}^{2(2n+1)-(k_1+k_2)} \cdot \sum_{k_4=0}^{2(2n+1)-(k_1+k_2+k_3)} \cdot \sum_{k_5=0}^{2(2n+1)-(k_1+k_2+k_3+k_4)} \cdot \sum_{k_6=0}^{2n+5-(6k_1+5k_2+4k_3+3k_4+2k_5)}$$

$$\frac{[2(2n+1)]! c_6^{k_1} c_5^{k_2+1} c_4^{k_3} c_3^{k_4} c_2^{k_5} c_1^{k_6}}{k_1! k_2! k_3! k_4! k_5! k_6! [2(2n+1)-k_1-k_2-k_3-k_4-k_5-k_6]!} \zeta^{-(4n+11)+2(6k_1+5k_2+4k_3+3k_4+2k_5+k_6)} +$$

$$\sum_{k_1=0}^{2(2n+1)} \cdot \sum_{k_2=0}^{2(2n+1)-k_1} \cdot \sum_{k_3=0}^{2(2n+1)-(k_1+k_2)} \cdot \sum_{k_4=0}^{2(2n+1)-(k_1+k_2+k_3)} \cdot \sum_{k_5=0}^{2(2n+1)-(k_1+k_2+k_3+k_4)} \cdot \sum_{k_6=0}^{2(n+3)-(6k_1+5k_2+4k_3+3k_4+2k_5)}$$

$$\frac{[2(2n+1)]! c_6^{k_1+1} c_5^{k_2} c_4^{k_3} c_3^{k_4} c_2^{k_5} c_1^{k_6}}{k_1! k_2! k_3! k_4! k_5! k_6! [2(2n+1)-k_1-k_2-k_3-k_4-k_5-k_6]!} \zeta^{-(4n+13)+2(6k_1+5k_2+4k_3+3k_4+2k_5+k_6)}$$

$$\begin{aligned}
 G_{4n+3}^{(0)}(\zeta) &:= P.P. \left[\left(\frac{1}{\zeta} + c_1 \zeta + c_2 \zeta^3 + c_3 \zeta^5 + c_4 \zeta^7 + c_5 \zeta^9 + c_6 \zeta^{11} \right)^{4n+3} \right] \\
 &= \sum_{k_1=0}^{4n+3} \cdot \sum_{k_2=0}^{4n+3-k_1} \cdot \sum_{k_3=0}^{4n+3-(k_1+k_2)} \cdot \sum_{k_4=0}^{4n+3-(k_1+k_2+k_3)} \cdot \sum_{k_5=0}^{4n+3-(k_1+k_2+k_3+k_4)} \cdot \sum_{k_6=0}^{2n+1-(6k_1+5k_2+4k_3+3k_4+2k_5)} \\
 &\quad \frac{(4n+3)! \cdot c_6^{k_1} c_5^{k_2} c_4^{k_3} c_3^{k_4} c_2^{k_5} c_1^{k_6}}{k_1! k_2! k_3! k_4! k_5! k_6! (4n+3-k_1-k_2-k_3-k_4-k_5-k_6)!} \zeta^{-(4n+3)+2(6k_1+5k_2+4k_3+3k_4+2k_5+k_6)} \\
 G_{4n}^{(\infty)}(\zeta) &:= P.P. \left[\left(\frac{1}{\zeta} + c_1 \zeta + c_2 \zeta^3 + c_3 \zeta^5 + c_4 \zeta^7 + c_5 \zeta^9 + c_6 \zeta^{11} \right) \left(\zeta + \frac{c_1}{\zeta} + \frac{c_2}{\zeta^3} + \frac{c_3}{\zeta^5} + \frac{c_4}{\zeta^7} + \frac{c_5}{\zeta^9} + \frac{c_6}{\zeta^{11}} \right)^{4n} \right] = \\
 &\quad \sum_{k_1=0}^{4n} \cdot \sum_{k_2=0}^{4n-k_1} \cdot \sum_{k_3=0}^{4n-(k_1+k_2)} \cdot \sum_{k_4=0}^{4n-(k_1+k_2+k_3)} \cdot \sum_{k_5=0}^{4n-(k_1+k_2+k_3+k_4)} \cdot \sum_{k_6=0}^{\frac{4n-1}{2}-(6k_1+5k_2+4k_3+3k_4+2k_5)} \\
 &\quad \frac{(4n)! \cdot c_6^{k_1} c_5^{k_2} c_4^{k_3} c_3^{k_4} c_2^{k_5} c_1^{k_6}}{k_1! k_2! k_3! k_4! k_5! k_6! (4n-k_1-k_2-k_3-k_4-k_5-k_6)!} \zeta^{4n-1-2(6k_1+5k_2+4k_3+3k_4+2k_5+k_6)} + \\
 &+ \sum_{k_1=0}^{4n} \cdot \sum_{k_2=0}^{4n-k_1} \cdot \sum_{k_3=0}^{4n-(k_1+k_2)} \cdot \sum_{k_4=0}^{4n-(k_1+k_2+k_3)} \cdot \sum_{k_5=0}^{4n-(k_1+k_2+k_3+k_4)} \cdot \sum_{k_6=0}^{\frac{4n+1}{2}-(6k_1+5k_2+4k_3+3k_4+2k_5)} \\
 &\quad \frac{(4n)! \cdot c_6^{k_1} c_5^{k_2} c_4^{k_3} c_3^{k_4} c_2^{k_5} c_1^{k_6+1}}{k_1! k_2! k_3! k_4! k_5! k_6! (4n-k_1-k_2-k_3-k_4-k_5-k_6)!} \zeta^{4n+1-2(6k_1+5k_2+4k_3+3k_4+2k_5+k_6)} + \\
 &\quad \sum_{k_1=0}^{4n} \cdot \sum_{k_2=0}^{4n-k_1} \cdot \sum_{k_3=0}^{4n-(k_1+k_2)} \cdot \sum_{k_4=0}^{4n-(k_1+k_2+k_3)} \cdot \sum_{k_5=0}^{4n-(k_1+k_2+k_3+k_4)} \cdot \sum_{k_6=0}^{\frac{4n+3}{2}-(6k_1+5k_2+4k_3+3k_4+2k_5)} \\
 &\quad \frac{(4n)! \cdot c_6^{k_1} c_5^{k_2} c_4^{k_3} c_3^{k_4} c_2^{k_5+1} c_1^{k_6}}{k_1! k_2! k_3! k_4! k_5! k_6! (4n-k_1-k_2-k_3-k_4-k_5-k_6)!} \zeta^{4n+3-2(6k_1+5k_2+4k_3+3k_4+2k_5+k_6)} + \\
 &\quad \sum_{k_1=0}^{4n} \cdot \sum_{k_2=0}^{4n-k_1} \cdot \sum_{k_3=0}^{4n-(k_1+k_2)} \cdot \sum_{k_4=0}^{4n-(k_1+k_2+k_3)} \cdot \sum_{k_5=0}^{4n-(k_1+k_2+k_3+k_4)} \cdot \sum_{k_6=0}^{\frac{4n+5}{2}-(6k_1+5k_2+4k_3+3k_4+2k_5)} \\
 &\quad \frac{(4n)! \cdot c_6^{k_1} c_5^{k_2} c_4^{k_3} c_3^{k_4+1} c_2^{k_5} c_1^{k_6}}{k_1! k_2! k_3! k_4! k_5! k_6! (4n-k_1-k_2-k_3-k_4-k_5-k_6)!} \zeta^{4n+5-2(6k_1+5k_2+4k_3+3k_4+2k_5+k_6)} + \\
 &\quad \sum_{k_1=0}^{4n} \cdot \sum_{k_2=0}^{4n-k_1} \cdot \sum_{k_3=0}^{4n-(k_1+k_2)} \cdot \sum_{k_4=0}^{4n-(k_1+k_2+k_3)} \cdot \sum_{k_5=0}^{4n-(k_1+k_2+k_3+k_4)} \cdot \sum_{k_6=0}^{\frac{4n+7}{2}-(6k_1+5k_2+4k_3+3k_4+2k_5)} \\
 &\quad \frac{(4n)! \cdot c_6^{k_1} c_5^{k_2} c_4^{k_3+1} c_3^{k_4} c_2^{k_5} c_1^{k_6}}{k_1! k_2! k_3! k_4! k_5! k_6! (4n-k_1-k_2-k_3-k_4-k_5-k_6)!} \zeta^{4n+7-2(6k_1+5k_2+4k_3+3k_4+2k_5+k_6)} + \\
 &\quad \sum_{k_1=0}^{4n} \cdot \sum_{k_2=0}^{4n-k_1} \cdot \sum_{k_3=0}^{4n-(k_1+k_2)} \cdot \sum_{k_4=0}^{4n-(k_1+k_2+k_3)} \cdot \sum_{k_5=0}^{4n-(k_1+k_2+k_3+k_4)} \cdot \sum_{k_6=0}^{\frac{4n+9}{2}-(6k_1+5k_2+4k_3+3k_4+2k_5)} \\
 &\quad \frac{(4n)! \cdot c_6^{k_1} c_5^{k_2+1} c_4^{k_3} c_3^{k_4} c_2^{k_5} c_1^{k_6}}{k_1! k_2! k_3! k_4! k_5! k_6! (4n-k_1-k_2-k_3-k_4-k_5-k_6)!} \zeta^{4n+9-2(6k_1+5k_2+4k_3+3k_4+2k_5+k_6)} + \\
 &\quad \sum_{k_1=0}^{4n} \cdot \sum_{k_2=0}^{4n-k_1} \cdot \sum_{k_3=0}^{4n-(k_1+k_2)} \cdot \sum_{k_4=0}^{4n-(k_1+k_2+k_3)} \cdot \sum_{k_5=0}^{4n-(k_1+k_2+k_3+k_4)} \cdot \sum_{k_6=0}^{\frac{4n+11}{2}-(6k_1+5k_2+4k_3+3k_4+2k_5)} \\
 &\quad \frac{(4n)! \cdot c_6^{k_1+1} c_5^{k_2} c_4^{k_3} c_3^{k_4} c_2^{k_5} c_1^{k_6}}{k_1! k_2! k_3! k_4! k_5! k_6! (4n-k_1-k_2-k_3-k_4-k_5-k_6)!} \zeta^{4n+11-2(6k_1+5k_2+4k_3+3k_4+2k_5+k_6)}
 \end{aligned}$$

$$\begin{aligned}
G_{2(2n+1)}^{(\infty)}(\zeta) := & P.P. \left[\left(\frac{1}{\zeta} + c_1 \zeta + c_2 \zeta^3 + c_3 \zeta^5 + c_4 \zeta^7 + c_5 \zeta^9 + c_6 \zeta^{11} \right) \left(\zeta + \frac{c_1}{\zeta} + \frac{c_2}{\zeta^3} + \frac{c_3}{\zeta^5} + \frac{c_4}{\zeta^7} + \frac{c_5}{\zeta^9} + \frac{c_6}{\zeta^{11}} \right)^{2(2n+1)} \right] = \\
& \sum_{k_1=0}^{2(2n+1)} \cdot \sum_{k_2=0}^{2(2n+1)-k_1} \cdot \sum_{k_3=0}^{2(2n+1)-(k_1+k_2)} \cdot \sum_{k_4=0}^{2(2n+1)-(k_1+k_2+k_3)} \cdot \sum_{k_5=0}^{2(2n+1)-(k_1+k_2+k_3+k_4)} \cdot \sum_{k_6=0}^{\frac{4n+1}{2} - (6k_1+5k_2+4k_3+3k_4+2k_5)} \\
& \frac{[2(2n+1)]! c_6^{k_1} c_5^{k_2} c_4^{k_3} c_3^{k_4} c_2^{k_5} c_1^{k_6}}{k_1! k_2! k_3! k_4! k_5! k_6! [2(2n+1) - k_1 - k_2 - k_3 - k_4 - k_5 - k_6]!} \zeta^{4n+1-2(6k_1+5k_2+4k_3+3k_4+2k_5+k_6)} + \\
& + \sum_{k_1=0}^{2(2n+1)} \cdot \sum_{k_2=0}^{2(2n+1)-k_1} \cdot \sum_{k_3=0}^{2(2n+1)-(k_1+k_2)} \cdot \sum_{k_4=0}^{2(2n+1)-(k_1+k_2+k_3)} \cdot \sum_{k_5=0}^{2(2n+1)-(k_1+k_2+k_3+k_4)} \cdot \sum_{k_6=0}^{\frac{4n+3}{2} - (6k_1+5k_2+4k_3+3k_4+2k_5)} \\
& \frac{[2(2n+1)]! c_6^{k_1} c_5^{k_2} c_4^{k_3} c_3^{k_4} c_2^{k_5} c_1^{k_6+1}}{k_1! k_2! k_3! k_4! k_5! k_6! [2(2n+1) - k_1 - k_2 - k_3 - k_4 - k_5 - k_6]!} \zeta^{4n+3-2(6k_1+5k_2+4k_3+3k_4+2k_5+k_6)} + \\
& + \sum_{k_1=0}^{2(2n+1)} \cdot \sum_{k_2=0}^{2(2n+1)-k_1} \cdot \sum_{k_3=0}^{2(2n+1)-(k_1+k_2)} \cdot \sum_{k_4=0}^{2(2n+1)-(k_1+k_2+k_3)} \cdot \sum_{k_5=0}^{2(2n+1)-(k_1+k_2+k_3+k_4)} \cdot \sum_{k_6=0}^{\frac{4n+5}{2} - (6k_1+5k_2+4k_3+3k_4+2k_5)} \\
& \frac{[2(2n+1)]! c_6^{k_1} c_5^{k_2} c_4^{k_3} c_3^{k_4} c_2^{k_5+1} c_1^{k_6}}{k_1! k_2! k_3! k_4! k_5! k_6! [2(2n+1) - k_1 - k_2 - k_3 - k_4 - k_5 - k_6]!} \zeta^{4n+5-2(6k_1+5k_2+4k_3+3k_4+2k_5+k_6)} + \\
& + \sum_{k_1=0}^{2(2n+1)} \cdot \sum_{k_2=0}^{2(2n+1)-k_1} \cdot \sum_{k_3=0}^{2(2n+1)-(k_1+k_2)} \cdot \sum_{k_4=0}^{2(2n+1)-(k_1+k_2+k_3)} \cdot \sum_{k_5=0}^{2(2n+1)-(k_1+k_2+k_3+k_4)} \cdot \sum_{k_6=0}^{\frac{4n+7}{2} - (6k_1+5k_2+4k_3+3k_4+2k_5)} \\
& \frac{[2(2n+1)]! c_6^{k_1} c_5^{k_2} c_4^{k_3} c_3^{k_4+1} c_2^{k_5} c_1^{k_6}}{k_1! k_2! k_3! k_4! k_5! k_6! [2(2n+1) - k_1 - k_2 - k_3 - k_4 - k_5 - k_6]!} \zeta^{4n+7-2(6k_1+5k_2+4k_3+3k_4+2k_5+k_6)} + \\
& + \sum_{k_1=0}^{2(2n+1)} \cdot \sum_{k_2=0}^{2(2n+1)-k_1} \cdot \sum_{k_3=0}^{2(2n+1)-(k_1+k_2)} \cdot \sum_{k_4=0}^{2(2n+1)-(k_1+k_2+k_3)} \cdot \sum_{k_5=0}^{2(2n+1)-(k_1+k_2+k_3+k_4)} \cdot \sum_{k_6=0}^{\frac{4n+9}{2} - (6k_1+5k_2+4k_3+3k_4+2k_5)} \\
& \frac{[2(2n+1)]! c_6^{k_1} c_5^{k_2} c_4^{k_3+1} c_3^{k_4} c_2^{k_5} c_1^{k_6}}{k_1! k_2! k_3! k_4! k_5! k_6! [2(2n+1) - k_1 - k_2 - k_3 - k_4 - k_5 - k_6]!} \zeta^{4n+9-2(6k_1+5k_2+4k_3+3k_4+2k_5+k_6)} + \\
& + \sum_{k_1=0}^{2(2n+1)} \cdot \sum_{k_2=0}^{2(2n+1)-k_1} \cdot \sum_{k_3=0}^{2(2n+1)-(k_1+k_2)} \cdot \sum_{k_4=0}^{2(2n+1)-(k_1+k_2+k_3)} \cdot \sum_{k_5=0}^{2(2n+1)-(k_1+k_2+k_3+k_4)} \cdot \sum_{k_6=0}^{\frac{4n+11}{2} - (6k_1+5k_2+4k_3+3k_4+2k_5)} \\
& \frac{[2(2n+1)]! c_6^{k_1} c_5^{k_2+1} c_4^{k_3} c_3^{k_4} c_2^{k_5} c_1^{k_6}}{k_1! k_2! k_3! k_4! k_5! k_6! [2(2n+1) - k_1 - k_2 - k_3 - k_4 - k_5 - k_6]!} \zeta^{4n+11-2(6k_1+5k_2+4k_3+3k_4+2k_5+k_6)} + \\
& + \sum_{k_1=0}^{2(2n+1)} \cdot \sum_{k_2=0}^{2(2n+1)-k_1} \cdot \sum_{k_3=0}^{2(2n+1)-(k_1+k_2)} \cdot \sum_{k_4=0}^{2(2n+1)-(k_1+k_2+k_3)} \cdot \sum_{k_5=0}^{2(2n+1)-(k_1+k_2+k_3+k_4)} \cdot \sum_{k_6=0}^{\frac{4n+13}{2} - (6k_1+5k_2+4k_3+3k_4+2k_5)} \\
& \frac{[2(2n+1)]! c_6^{k_1+1} c_5^{k_2} c_4^{k_3} c_3^{k_4} c_2^{k_5} c_1^{k_6}}{k_1! k_2! k_3! k_4! k_5! k_6! [2(2n+1) - k_1 - k_2 - k_3 - k_4 - k_5 - k_6]!} \zeta^{4n+13-2(6k_1+5k_2+4k_3+3k_4+2k_5+k_6)}
\end{aligned}$$

References

- ASTM (2014) E399-12e3 Standard test method for linear-elastic plane-strain fracture toughness K_{Ic} of metallic materials. ASTM volume 03.01: Metals-Mechanical Testing; Elevated and Low-Temperature Tests; Metallography
- Atkinson C, Smelser RE, Sanchez J (1982) Combined mode fracture via the cracked Brazilian disk test. *Int J Fracture* 18:279–291
- Awaji H, Sato S (1978) Combined mode fracture toughness measurement by the disk test. *J Eng Mater T ASME* 100:175–182
- Bluhm JI (1975) Slice synthesis of a three dimensional work of fracture specimen. *Eng Fract Mech* 7:593–604
- Burniston EE (1969) An example of a partially closed Griffith crack. *Int J Rock Mech Min* 5:17–24
- Carolan D, Alveen P, Ivankovic A, Murphy N (2011) Effect of notch root radius on fracture toughness of polycrystalline cubic boron nitride. *Eng Fract Mech* 78:2885–2895
- Creager JM, Paris P (1967) Elastic field equation for blunt cracks with reference to stress corrosion cracking. *Int J Fract* 3:247–252

- Dong S (2008) Theoretical analysis of the effects of relative crack length and loading angle on the experimental results for the cracked Brazilian disk testing. *Eng Fract Mech* 75:2575–2581
- Erarslan N (2013) A study on the evaluation of the fracture process zone in CCNBD rock samples. *Exp Mech* 53:1475–1489
- Fowell RJ, Xu C (1993) The cracked chevron notched Brazilian disc test- Geometrical considerations for practical rock fracture toughness measurement. *Int J Rock Mech Min Sci Geomech Abstr* 30(7):821–824
- Fowell RJ, Xu C, Dowd PA (2006) An update on the fracture toughness testing methods related to cracked CCNBD specimen. *Pure appl Geophys* 163:1046–1057
- Iqbal MJ, Mohanty B (2006) Experimental calibration of stress intensity factor of the ISRM suggested CCNBD specimen used for the determination of mode-I fracture toughness. *Int J Rock Mech Min* 43:57–64
- Iqbal MJ, Mohanty B (2007) Experimental calibration of ISRM suggested fracture toughness measurement techniques in selected brittle rocks. *Rock Mech Rock Eng* 40(5):453–475
- ISRM (1978) Suggested methods for determining tensile strength of rock materials. *Int J Rock Mech Min Sci Geomech Abstr* 15(3):99–103
- ISRM (Coordinator Fowell RJ) (1995) Suggested methods for determining mode-I fracture toughness using CCNBD specimens. *Int J Rock Mech Min* 32(1):57–64
- ISRM (Coordinator Ouchterlony F) (1988) Suggested methods for determining the fracture toughness of rock. *Int J Rock Mech Min* 25(2):71–96
- Kolhe R, Hui Chung-Yuen, Zehnder AT (1998) Effects of finite notch width on the fracture of chevron-notched specimens. *Int J Fract* 94:189–198
- Kolosov GV (1935) Application of the complex variable to the theory of elasticity (in Russian), ONTI. Moscow-Leningrad
- Kourkoulis SK, Markides ChF, Chatzistergos PE (2012) The standardized Brazilian disc test as a contact problem. *Int J Rock Mech Min* 57:132–141
- Kourkoulis SK, Markides ChF, Pasiou ED (2015a) A combined analytic and experimental study of the displacement field in a circular ring. *Meccanica* 50(2):493–515
- Kourkoulis SK, Markides ChF, Chatzistergos PE (2015b) Numerical analysis of the disc-jaw interface during the standardized implementation of the Brazilian-disc test. In: Pelekasis N, Stavroulakis G (eds) 8th GRACM international congress on computational mechanics. University of Thessaly Press, Volos, Greece, p. 58
- Lin H, Xiong W, Xiong Z, Gong F (2015) Three-dimensional effects in a flattened Brazilian disk test. *Int J Rock Mech Min* 74:10–14
- Markides ChF, Kourkoulis SK (2012) The Stress Field in a standardized Brazilian disc: the influence of the loading type acting on the actual contact length. *Rock Mech Rock Eng* 45(2):145–158
- Markides ChF, Kourkoulis SK (2014a) Stresses and displacements in an elliptically perforated circular disc under radial pressure. *Eng Trans* 62(2):131–169
- Markides ChF, Kourkoulis SK (2014b) The finite circular disc with a central elliptic hole under parabolic pressure. *Acta Mech* 226(6):1929–1955
- Markides ChF, Kourkoulis SK (2015a) The circular disc under rotational moment and friction: application to the cracked Brazilian-disc test. *Arch Appl Mech*. doi:10.1007/s00419-015-1023-6 (to appear)
- Markides ChF, Kourkoulis SK (2015b) The displacement field in a finite circular disc with a central rectangular slit. *Procedia Eng* 109:257–267. doi:10.1016/j.proeng.2015.06.231
- Markides ChF, Pazis DN, Kourkoulis SK (2011) Stress intensity factors for the Brazilian disc with a short central crack: opening versus closing cracks. *Appl Math Model* 35(12):5636–5651
- Munz D, Bubsey RT, Srawley JE (1980) Compliance and stress intensity coefficients for short bar specimens with chevron notches. *Int J Fract* 16(4):359–374
- Muskhelishvili NI (1963) Some basic problems of the mathematical theory of elasticity. Noordhoff, Groningen
- Pazis DN, Theocaris PS, Konstantellos BD (1988) Elastic overlapping of the crack flanks under mixed-mode loading. *Int J Fract* 37:303–319
- Rooke DP, Tweed J (1973) The stress intensity factors of a radial crack in a point loaded disc. *Int J Eng Sci* 11:285–290
- Savin GN (1970) Stress distribution around holes, NASA, TT F-607. Washington DC
- Shetty DK, Rosenfield AR, Duckworth WH (1987) Mixed mode fracture in biaxial stress state: application of the diametral-compression (Brazilian disk) test. *Eng Fract Mech* 26:825–840
- Sinclair GB, Kondo M (1984) On the stress concentration at sharp re-entrant corners in plates. *Int J Mech Sci* 26(9/10):477–487
- Theocaris PS (1991) Peculiarities of the artificial crack. *Eng Fract Mech* 38(1):37–54
- Theocaris PS, Petrou L (1987) The order of singularities and the stress intensity factors near corners of regular polygonal holes. *Int J Eng Sci* 25(7):821–832
- Theocaris PS, Petrou L (1988) The influence of the shape and curvature of crack fronts on the values of the order of singularity and the stress intensity factor. *Acta Mech* 72:73–94
- Theocaris PS, Petrou L (1989) From the rectangular hole to the ideal crack. *Int J Solids Struct* 15(3):213–233
- Timoshenko SP, Goodier JN (1970) Theory of elasticity, 3rd edn. McGraw-Hill, New York
- Tweed J (1970) The determination of the stress intensity factor of a partially closed Griffith crack. *Int J Eng Sci* 8:793–803
- Wang QZ (2010) Formula for calculating the critical stress intensity factor in rock fracture toughness tests using CCNBD specimens. *Int J Rock Mech Min* 47:1006–1011
- Wang QZ, Xing L (1999) Determination of fracture toughness K_{IC} by using the flattened Brazilian disk specimen for rocks. *Eng Fract Mech* 64:193–201
- Wang QZ, Jia XM, Kou SQ, Zhang ZX, Lindqvist PA (2004a) The flattened Brazilian disc specimen used for testing elastic modulus, tensile strength and fracture toughness of brittle rocks: analytical and numerical results. *Int J Rock Mech Min* 41:245–253
- Wang QZ, Jia XM, Wu LZ (2004b) Wide-range stress intensity factors for the ISRM suggested method using CCNBD specimens for rock fracture toughness tests. *Int J Rock Mech Min* 41:709–716
- Wang QZ, Gou XP, Fan H (2012) The minimum dimensionless stress intensity factor and its upper bound for CCNBD fracture toughness specimen analyzed with straight through crack assumption. *Eng Fract Mech* 82:1–8
- Wang QZ, Fan H, Gou XP, Zhang S (2013) Recalibration and clarification of the formula applied to the ISRM-suggested CCNBD specimens for testing rock fracture toughness. *Rock Mech Rock Eng* 46:303–313